**Article:**
Jenkins, J., Gilbert, M., Fatima, N. et al. (Accepted: 2026) In-tissue structural biology of the brain: a focus on Alzheimer's disease pathology. Methods in Enzymology. ISSN: 0076-6879 (In Press)

**Word count:** 11,897

**Title:** In-tissue structural biology of the brain: a focus on Alzheimer's disease pathology.

**Authors**: Joshua Jenkins, Madeleine Gilbert, Nayab Fatima, Thomas O'Sullivan, William Thompson, Rene Frank

**Abstract**

The structure of biology spans length scales from meters to Ångstroms – from whole organisms to the atomic positions of macromolecules. Cryo-electron microscopy is well-established for determining the structures of individual macromolecules in isolation, including pathological aggregates from post-mortem donor Alzheimer's disease brain. Recent advances integrating cryo-fluorescence microscopy, sample preparation and cryo-electron tomography are revealing macromolecular structures in the context of cells and anatomically intact tissues. In this chapter, we describe experimental workflows for targeting the in-tissue structure of Alzheimer's disease pathology. We discuss associated practical considerations and limitations of fluorescence labelling, vitrification, sample thinning by cryo-ultramicrotomy and cryo-focused ion-beam scanning electron microscopy (cryoFIB-SEM), cryogenic correlated light and electron microscopy (cryoCLEM), cryo-electron tomography (cryoET) and in-tissue subtomogram averaging (STA). These experimental considerations may be useful and applicable to amyloids, diseases and fundamental structural biology research questions more broadly.

**Key words:**
Cryo-electron tomography (cryo-ET); neuropathology; cryogenic correlated light and electron microscopy (cryo-CLEM); in situ structure; Alzheimer's disease; amyloid.

## 1. Introduction

### 1.1 Neurological disease and amyloid

The scale, structure and function of the human central nervous system is highly complex, composed of ~86 billion neurons and ~460 cell types [1,2] that exert control over most physiological functions, and are vital to cognition [3]. Neurological disorders present in the clinic with defining sensory, cognitive and/or motor symptoms but the underlying pathological mechanisms of most neurological conditions, including dementia, remains unclear [4,5].

Alzheimer's disease and related dementias are characterised by the abnormal deposition of amyloids composed of Aβ, tau, α-synuclein and TDP-43 [6]. Collectively, these neuropathologies cause the most prevalent neurodegenerative diseases, including AD, cerebral amyloid angiopathy (CAA), Parkinson's disease dementia (PDD), dementia with Lewy bodies (DLB), and frontotemporal dementia (FTD) [5,7–12]. Longitudinal studies of these diseases indicate that neuropathology precedes cognitive symptoms and spreads by prion-like mechanisms within the brain [13,14]. Currently, no treatment is available that prevents AD but recent FDA-approved Aβ immunotherapeutics (lecanemab and donanemab) delay AD progression by 4-6 months [15,16].

### 1.2 Structural biology of amyloids from neurodegenerative disease

Early structural studies showed that different proteinaceous deposits characteristic of distinct neurodegenerative diseases comprise amyloid filaments, defined by a cross-β-sheet structure [17–20]. X-ray crystallography, solid-state NMR and cryoEM reconstructions of in vitro assembled

amyloids have revealed many different structures [21–24]. More recently, pioneering single-particle cryoEM studies of amyloids (composed of Aβ, tau, α-synuclein, or TDP-43) bulk purified from late-stage post-mortem donor brains indicate these proteins form disease-specific structures [25]. For example, tau filaments extracted from postmortem donor brain samples with different neurodegenerative tauopathies exhibit divergent tau folds [26–31]. These structural studies suggest a limited number of different disease-specific amyloid folds are conserved in patients with the same disease [25].

Importantly, the structures of amyloids purified from patient donor brain were not predicted from earlier structures of amyloid prepared in vitro [32,33]. Similarly, amyloid purified from some, but not all, animal models have a structure that differs from that of amyloid purified from human donor brain [34–38]. This implies that chemical and/or biological factors, absent from some in vitro preparations and some models, but present within patient human brain, affect the structure of pathological amyloids. For therapeutic development, it may therefore be important that animal or cell models recapitulate the same pathological structures as those found in human patient brain [32,33]. Amyloid purification from tissues by both detergent extraction or mild tissue soaking preparations [39] does not recover all the amyloid present within patient donor brain tissue and it is also possible that not all amyloid structures can withstand the rigour of extraction and purification. The question therefore remains to what extent disease-specific amyloid folds solved from purified postmortem brain tissues are characteristic of the population of structures present within intact postmortem brain tissues.

## 2. In situ structural biology

It is now possible to address the question of amyloid structure within intact cells and tissues by in situ cryo-electron tomography (cryoET) [40]. Technological advances in cell and tissue sample preparation, direct electron detectors, and software developments have underpinned recent advances in cryoET and herald a new wave in structural biology revealing the in situ structure of macromolecules [41–44]. In situ structural biology has the potential to go beyond the cryoEM 'resolution revolution' [45], imaging and integrating across length-scales – from the structure of macromolecules to cells, tissues and whole organisms (**Fig. 1**)[43,44,46–48]. In this context, one can glean how the constellation of macromolecular complexes, organelles and cells mediate biological function and pathological mechanisms in disease. This approach necessitates combining expertise beyond the traditional partnership of structural biologists and biochemists to include cell biologists, physiologists and clinicians. There is also the opportunity for experiments to become unified across disciplines by starting with experiments that test function and activity within living cells, tissues, and animals, and are followed by subsequent direct correlation to in situ structural information in the same specimen. In the following sections we will outline some of the practical considerations and limitations in pursuing in situ structural biology experiments [47–49]. There are several key steps that can be broadly separated into five categories: live cell/tissue labelling, vitrification, sample thinning and cryo-fluorescence microscopy, cryoET data collection, and STA.

### 2.1 Live cell/tissue labelling

Most proteins occupy only a tiny fraction of the total volume of biological specimens and are often concentrated, for example within specialized subcellular compartments and organelles [50–52]. Each tomogram also only captures a small subvolume (~0.1 $\mu m^3$) of the specimen (**Fig. 1**). Therefore, labels capable of pinpointing the precise location of target proteins are usually essential, otherwise the proportion of tomograms that contain the molecule of interest will either be very low, or even absent. Imaging fluorescent labels is ideally suited for guiding cryoET data

collection because light microscopy can locate targets at submicron resolution across large cell and tissue samples [53].

Since cryoET is usually performed with native biological specimens that have not been chemically fixed or permeabilised, only labelling methods compatible with live-cell imaging, including genetically encoded fluorescent protein tags [50,51], or small molecular fluorescent ligands, can be considered (**Fig. 3**). Ideally, fluorescence labels are validated to gauge the selectivity and sensitivity of the label by immunofluorescence (**Fig. 4**). It is also important that the label and its mode of delivery to the target is benign, having a minimal effect on specimen viability and biological function. For example, utilising well-established buffer and perfusion protocols [54,55] for maintaining the viability of brain tissue slice preparations (**Fig. 5**).

**2.2 Vitrification**

Vitrification is a necessary and defining step of all cryoEM and cryoET methods in which biological samples are suspended in their native aqueous environment, freezing the liquid water within cells and tissues in an amorphous, liquid state, whilst avoiding crystalline ice formation [56]. This differs from sample preparation methods used for room-temperature, resin-embedded EM by avoiding chemical fixation or freeze-substitution into harsh organic solvents and heavy metal staining that require dehydrating biological samples causing shrinkage and/or protein denaturation, and the washing away of cellular proteins [57].

For cells cultured on EM grids that are ~5 µm thick, vitrification can be achieved by plunge-freezing in a liquid ethane cryogen and cryo-protectants [56,58]. However, for tissues which are much thicker, complete vitrification by plunge-freezing is not possible because the freezing rate deeper in the specimen is too slow. Instead, the vitrification of tissue biopsies up to 200 µm thick can be achieved using high-pressure freezing (HPF) [59]. During this transition the sample is rapidly cooled to -196° C within ~20 ms by a jet of liquid nitrogen whilst under ~2100 bar pressure, after which the sample is returned to atmospheric pressure and kept at below the devitrification temperature (-150° C) for all subsequent stages of the work (**Fig. 6**). The theoretical basis of HPF comes from the observation that water expands during the transition from liquid to crystalline ice (**Fig. 6**). Applying high external pressure opposes the volume expansion of water molecules necessary to form crystalline water during freezing, effectively lowering the rate of ice formation to achieve complete vitrification of thicker samples.

To prepare tissues, 100-300 µm slices are cut with a vibratome, following protocols well established for in vitro slice electrophysiology [54]. Biopsies (1-2 mm diameter) are then collected from tissue slices and soaked in cryo-protectants before HPF, which further lowers the rate of ice formation such that the biopsy is vitrified at liquid nitrogen temperatures before ice crystals can grow [60]. It is important to consider if the addition of cryo-protectants could have detrimental effects on the native structure of tissues, for example by exerting osmotic pressure. High molecular weight dextran in particular has been demonstrated to have little osmotic effect on tissues [60,61], whilst still facilitating robust tissue vitrification [37,47,60,62]. On the other hand, not all tissue types vitrify robustly under the same conditions [63]. Though yet to be verified experimentally, this is probably in part because of the different solute composition of different cells affecting the rate of crystalline ice formation.

Optimising slice preparation and vitrification conditions is challenging and not currently amenable to high throughput screening because the extent of sample vitrification can only be accurately assessed on the electron microscope after labour-intensive sample preparation. Additionally, devitrification can ruin the sample during steps between HPF and cryoEM data

collection. Crystalline ice in non-vitreous regions of the sample produce Bragg reflections that can be definitively assessed by imaging in diffraction mode (with a selected area aperture). The vitrification status of a sample can be more straightforwardly detected in cryoET tilt-series, with regions of the sample that are non-vitreous/devitrified displaying starkly varying contrast in micrographs collected at different tilts (**Fig. 7**). Varying degrees of partial devitrification can also arise in which some regions of cells are vitreous, adjacent to other regions that are non-vitreous or devitrified, and that may be hidden in reconstructed tomographic volumes (**Fig. 7**). Consequently, quality control of all tilt series collected, to verify complete vitrification is essential [64], before further structural interpretation and analysis of cryoET datasets is possible.

Overall, sample preparation and vitrification can be a trade-off between maintaining the native state whilst still enabling robust vitrification. When optimising sample preparation, the effect of this trade-off on cellular function and viability should also be considered.

**2.2 Sample thinning and cryo-fluorescence microscopy**

Tissues and most cells are too thick to be directly imaged by current transmission EM microscopes [65,66]. Consequently, cryo-preserved specimens must be thinned. Cryo-ultramicrotomy uses a diamond knife to trim a stub of the sample, from which ~50-150 nm thick serial cryo-sections are cut [67] (McDowall et al., 1983, Al-Amoudi et al., 2004) (**Fig. 8**). As a cryo-section is cleaved from the tissue stub, its leading face adheres to the rear edge of the previous cryo-section, generating a ribbon of serial vitreous tissue cryo-sections that can be manoeuvred and placed flat on a glow-discharged EM grid with the aid of a gold eyelash controlled by a micromanipulator [68] (**Fig. 9**). The tissue ribbon is adhered securely to the carbon support-film using an electrostatic gun [69]. Manual micromanipulation of tissue ribbons and attachment to EM grids are the most technically challenging aspects of cryo-ultramicrotomy.

Alternative thinning methods are now established, [70] leveraging cryo-focused ion-beam scanning electron microscope (cryoFIB-SEM) technology developed in material science [71]. Samples are thinned using a focused beam of ions to ablate targeted areas of the sample, leaving behind a thinned lamella of the sample [70,72]. To prepare tissue lamellae, a series of trenches are milled into the sample to expose a tissue chunk (~10 µm thick)[73–76] (**Fig. 10**). The tissue chunk is then adhered to a needle by metal re-deposition, detached, and lifted out of the carrier using a micromanipulator [73,74,76,77]. The tissue chunk is then transferred to an EM grid where it is adhered at one or more edges of an EM grid. Prior cryo-planing of the HPF sample by cryo-ultramicrotomy to remove the top 2-10 µm of tissue can improve the success of liftout by removing ice contamination and providing a cleaner surface for FIB-milling [72](**Fig. 11**). After liftout, the EM grid-attached tissue chunk is thinned further until a 100-300 nm lamella is generated (**Fig. 12**). The yield of liftout lamellae is relatively low and the major challenges are the fragility of lamellae during transfer from the cryoFIB-SEM to cryoEM and ice contamination that accumulates on the surface of lamellae either in the cryoFIB-SEM or during transfer to cryoEM. The latter can be much reduced by using a low-humidity chamber [78]. Lifting out very large tissue chunks and milling this into multiple sub-chunks is an elegant approach to increase the yield of liftout lamellae [79,80].

We estimate cryo-ultramicrotomy currently generates a >100-fold higher yield of thinned sample compared to cryoFIB-milling lift-out. This throughput is an important consideration for generating sufficient numbers of cryo-electron tomograms for representative datasets, and sufficient target particles for high-resolution subtomogram averaging (STA). Importantly, both cryo-ultramicrotomy and cryoFIB-SEM result in varying degrees of sample damage. In cryo-ultramicrotomy, the diamond knife can cause deformation of the specimen, including ‘crevices’

in which sub-regions of the vitreous cryo-section are torn [81]. Crevices are relatively rare except if the diamond knife is blunt or damaged (**Fig. 13**). Since the HPF specimens are non-crystalline and behave as a viscous liquid, the mechanical force of sectioning can move or deform the sample, causing membranes and subcellular compartments to change their shape along the cutting direction of the knife. This deformation is localised and variable (**Fig. 13**). Knife damage has been referred to as 'compression' but this term may not be accurate since aqueous solutes are not compressible by the force applied during ultramicrotomy [82]. Localised deformation of vitrified liquids in the sample along the cutting direction must be considered when quantifying the shape of organelles and subcellular compartments. Remarkably, proteins within vitreous cryo-sections remain intact from which high-resolution in situ structures can be determined, for example resolving the polypeptide fold of tau filaments [40], and even reaching high resolution [83,84].

FIB-milling has the advantage of avoiding deformation but instead damages the sample by amorphization of the top and bottom ~60 nm layer throughout the thinned sample [85–87]. This is caused by the ion beam that in the process of milling the sample collides with and penetrates the tissue surface, generating a collision cascade that leads to damage and a loss of high-resolution structural information in the sample. Additional cryo-protectants, such as sucrose, may also be necessary before HPF to avoid partial devitrification during cryoFIB-milling [40,79,88,89].

To locate and guide sample thinning and the collection of in situ cryoET data, fluorescent labels in vitrified cells and tissues are imaged by cryo-fluorescence microscopy (cryoFM). These microscopes use a cryo-stage to maintain samples at <150° C and an air objective lens for wide-field [90–92], confocal [93] or super-resolution [94–96] imaging. CryoFM is initially performed before thinning with test and control samples to validate the specificity of live cell/tissue labelling (as outlined in section 2.1), including identifying autofluorescence that can interfere with the detection of fluorescent labels [97]. Bright field or reflection images may also be collected to mark fiducial features within the sample and/or the outer rim of the HPF carrier to triangulate where the targets are within the sample (**Fig. 14**). Following successful production of vitreous tissue cryo-sections or lamellae, cryoFM images of the specimen can be collected to validate the targeting of sample thinning and guide the collection of cryoET datasets. CryoFM has been integrated into cryo-ultramicrotome and cryoFIB-SEM instruments, albeit these instruments are currently limited to wide-field fluorescence microscopes [98].

## 3. CryoCLEM-guided in situ cryoET data collection

CryoET involves selecting regions of the thinned specimen to collect a series of 2D cryoEM micrographs at varying tilts of the stage, from which a 3D tomographic volume is reconstructed [41,99,100]. To target the collection of these data by cryogenic correlated light and electron microscopy (cryoCLEM) [92], cryoFM images of the specimen are aligned to medium magnification (~50 Å pixel size) cryoEM images of the specimen.

### 3.1 CryoET

CryoET data collection considers several limitations: 1) radiation damage [101–103], resulting in the first image containing more information than the last , 2) radiation induced motion of the sample [104–107] , and 3) the path length through the specimen, which increases at higher tilts. Consequently, most cryoET datasets are collected from low to high tilt (0 to +/-60°) [108] in 1-3° tilt increments (1-2 e/Å$^2$ dose, 1-3 Å pixel size) [109], acquired as movie frames [105,106]. Images are collected under focus to increase image contrast to be able to identify individual

macromolecules [110]. However, delocalisation of high frequency spatial information at high defocus should be considered [111,112]. Recent advances in microscope hardware and software have dramatically increased the speed and quality of cryoET data collection [113,114] and widened the field of view [115,116] . Hybrid cryoET data collection or template matching in single-particle analysis (SPA) cryoEM datasets is an alternative approach to obtaining high-resolution in situ structures [117–120].

### 3.2 Image processing

To reconstruct tomograms, movie frames of each tilt increment are aligned and summed [121] before the tilt series is next aligned and reconstructed, most commonly by weighted back projection methods [122–124]. Recent developments in computational processing software packages have enabled large datasets to be efficiently reconstructed in a more automated fashion [125–127].

CryoET datasets provide raw 3D molecular resolution maps of the sample revealing a label-free, native molecular architecture of cells and tissues. Since cells and tissues are highly crowded and heterogeneous, identifying macromolecular constituents within tomograms is time consuming and challenging. Larger macromolecular assemblies including the lipid bilayer of the plasma membrane and some intracellular organelles, ribosomes, proteosomes, and microtubules often can be directly and unambiguously identified. Topological features can be deduced using prior knowledge, for example in assigning intra- versus extracellular locations either side of a plasma membrane in the tomogram based on the distribution of organelles in the tomogram. Manual, semi-supervised or fully automated 3D segmentations of identifiable constituents within tomograms provide important contextual information, for example the density and geometric arrangement of macromolecular assemblies that can provide a structural framework for understanding complex mechanisms [40,62,128–131]. For large cryoET datasets training machine learning models can accelerate the detection and segmentation of some constituents, including membranes [132–134].

Although raw cryoET reconstructions provide direct insights, the 2-4 nm resolution of these maps [135]is currently insufficient to catalogue all proteins in each tomogram, and furthermore, many features untargeted by cryoCLEM are scarce. Given the varying quality and confidence in assigning constituents within cryoET datasets, it is valuable to report summary information for each tomogram, tabulating the identification and prevalence of constituents, as well as defining inclusion and exclusion criteria. For example, since there are a myriad of different filamentous proteins in almost all cells, initially identifying pathological amyloid within raw in situ cryoET data requires validation by cryoCLEM [37,40]. This is achieved by computational alignment of tomographic volumes to medium magnification cryoEM and cryoFM images [136–139] to confirm if and where within the cryoET dataset the target protein was acquired. This targeted approach supports a definitive identification of in situ constituents of tomograms, which can be achieved by STA.

## 4. Subtomogram averaging

Macromolecular structure determination is the primary objective of STA. As for single particle cryoEM, there are several parameters that influence the attainable resolution, including sample thickness, particle copy number, tilt series alignment, and image preprocessing [140]. Several subtomogram averaging packages have been used for high-resolution STA [125,141–145]. Achieving high resolution most efficiently requires accurately modelling and correcting for sample motion and deformations caused by the electron beam, uncertainties in the tilt-scheme

geometry and electron-optical aberrations [125]. In Warp/M, these parameters are simultaneously refined using gradient-descent optimisation, which treats each particle within a cryo-electron tomogram as part of the same deformable system, rather than optimising each particle parameter independently [126].

### 4.1 Modelling amyloid filaments

Subtomogram averaging requires first marking the coordinate locations and orientation of a target macromolecular complex ('particle' or 'subtomogram') within reconstructed tomograms. Multiple picking strategies have been implemented to estimate the position and orientation of each macromolecule, that include manual picking, template matching and machine learning approaches [122,146–150]. There are also algorithms that use Morse theory to define topological relationships of varying tomographic density for particle picking [151].

The method used for STA particle picking is informed by the macromolecule of interest. For example, ribonucleoproteins are efficiently identified and picked using template matching [152] and machine learning approaches [153]. To model the complex organisations of amyloid filaments, manual picking is currently most reliable using several GUI-based applications that have filament tracing functionality [122,146,147,150,154,155]. Amyloid filament paths and orientations can be initially estimated by placing model coordinates at the start and end of each filament, ensuring the contour path of each pair of coordinates is accurately aligned to the helical axis (**Fig. 15**).

### 4.2 Considerations for amyloid subtomogram alignment

Several approaches to subtomogram alignment and averaging have been developed. The first used angular searching and fast rotational matching alignment procedures to calculate the rotational and translational shifts required to maximize the cross-correlation (CC) between a subtomogram and a reference, these transformations are applied to all subtomograms to generate an averaged map with higher signal-to-noise ratio (SNR) [146,156–158]. The higher SNR map is then used as an updated reference for subsequent iterations of refinement. In contrast to CC, maximum-likelihood STA use estimates of the probability of observing each subtomogram orientation for a given reference and refines this weighting [159,160]. More recently, regularized-likelihood, an elegant Bayesian framework, has been developed that uses prior information and the observed data to search for STA alignment with the highest probability of being correct [161]. In depth discussion of the theoretical principles of STA, along with general considerations for generating initial references, masking, and particle box size are well-described elsewhere [124,126,161,162], see also filament-specific protocols [163].

For in-tissue structural studies of amyloids, knowledge about the symmetry is useful [164,165]. Amyloid filaments comprise repeating units of identical polypeptide folds (monomers), stacked perpendicular to the filament axis, each repeating unit is separated by 4.8 Å (helical rise) [20] and is rotated relative to its neighbouring units (helical twist, between -180° and +180°). Helical twist and rise are used to describe the helical symmetry of amyloids [26]. Initially, STA in PEET [158,166] with a box size that encompasses each, whole filament generates an average from which the helical twist of filaments in situ can be estimated (**Fig. 15**) and used for subsequent helical reconstruction methods in RELION [167,168]. To determine the structure of the underlying repeating unit, the helical axis of each filament is subsampled at intervals, increasing the copy number of subtomograms from 10-100 to many thousands per tomogram for helical averaging in RELION [168]. In single particle analysis, amyloid filaments are usually positioned

horizontally within a thin film of ice such that the filament axis is approximately perpendicular to the projection axis. In cryoET of cells and tissues, filament orientations are unconstrained by a film of ice [40]. Consequently, it is important to consider the orientation of the helical axis within the 3D volume to ensure the most accurate estimation of parameters that are needed for helical reconstruction in RELION [26,167]. These include the tilt, which describes the out-of-plane orientation of the filament within the sample and is modelled as a mono-modal Gaussian on the tilt angle. The psi parameter describes the in-plane rotation of the filament and is modelled by a bi-modal Gaussian on the psi angle. Finally, the in-plane translations perpendicular and parallel to the helical axis are described for translational searches. Providing an initial estimate of these angular parameters significantly reduces the search range that needs to be sampled to generate a *de novo* reference.

### 4.3 Identifying amyloid heterogeneity by classification

Heterogeneity may exist in the conformation and constituents of macromolecular assemblies in situ. Resolving and quantifying macromolecular heterogeneity within cells and tissues is an exciting frontier of in-situ structural biology and is advancing our understanding of broad biological mechanisms [40,169–173].

Structural heterogeneity of amyloid can be considered at multiple levels. 1) At the primary structural level of amino acids, including post-translational modifications [174,175]. 2) The backbone structure of the monomer subunit in the ordered core of the filament that defines the amyloid fold (Fitzpatrick et al., 2017). 3) Structural variation of quaternary contacts between pairs of monomer subunits in filaments composed of multiple protofilaments, which gives rise to ultrastructural polymorphs [26,176]. For example, AD tau filaments are composed of two protofilaments with identical C-shaped folds that form two different ultrastructural polymorphs (paired helical filament (PHF) and straight filament (SF) with distinct quaternary interactions [26,176]. In-tissue subtomogram averaging to date has resolved the amyloid fold and structural heterogeneity at the level of ultrastructural polymorphs, and variations in helical twist [40].
Discrete classification methods that group subtomograms into a predefined number of classes can be used to identify amyloid heterogeneity in tissue (**Fig. 15**). Using 3D classification in RELION [168,177], tau threads within AD post-mortem human brain tissue contained both PHF and SF filaments, resolved to 18 Å resolution [40].

### 4.4 Structure validation

Validation of the accuracy of a model and its fit to the experimental data is an important consideration [178–182]. STA is capable of producing maps with sufficient resolution ($\lesssim$5 Å) in which the shape of some amino acids in the polypeptide chain can be distinguished and an atomic model can be unambiguously built, using prior bond distance and angle restraints [183]. In such circumstances, Q-scores, a type of per-atom map-model cross-correlation, provides an excellent metric for cryoEM map validation [184,185]. In practice, attaining such near-atomic resolution by STA is often limited by the number of particles [186], resulting in intermediate (5-12 Å) resolution structures, in which atomic positions are unresolved but the separation of secondary structural elements of the polypeptide chain can be observed. Depending on the resolution of the map, the shape and size of the macromolecule, and if candidate atomic models are available, it may be possible to confirm the identity of the protein by rigid model-map fitting. However, real space fitting models into intermediate resolution maps is fraught with risk because the CC fitting score does not explicitly estimate signal and error in the map. Additionally, since a CC score is not an absolute metric, comparing candidate models is not possible. To address this,

recent model-map fitting tools, em_placement or emplace_local, build on maximum likelihood scoring, well-established for molecular replacement searches in X-ray crystallography data, to estimate the signal and error in the map and to what extent the model explains the map [187–189]. Emplace_local likelihood gain score is an absolute metric of the fit of a model (**Fig. 15**), through which competing hypotheses of what model is a better fit can also be assessed, for example distinguishing between different tau filament ultrastructural polymorphs in situ [40,189].

### 4.5 Future directions

Exciting, long-term developments in cryoEM instrumentation are afoot, including laser phase plates [190–193], ptytography/4D-STEM [194,195], chromatic aberration correctors [196], and imaging at helium temperatures [197]. With further improvements, raw tomographic volumes may well be generated that reach intermediate resolution. Many more individual macromolecular complexes would be identifiable, particularly in thicker in-cell or tissue specimens, for which an absolute model-map score, such as em_placement, is likely important [187,188].

Advances in complementary in situ structural methods imaging wider and deeper fields of view at lower resolution, including volumetric cryoFIB-SEM [198,199] and cryo-soft X-ray tomography [200–202] can provide additional label free, in situ contextual information [203,204]. Similarly, compositional spectroscopic imaging by electron energy loss spectroscopy (EELS) and energy dispersive X-ray spectroscopy (EDX) [205,206], secondary ion mass spectrometry (SIMS) [207,208] are being explored in vitrified cells and tissues. Integrating in situ cryoCLEM-guided cryo-ET with complementary methods on the same specimen is challenging and could be particularly useful for deciphering molecular mechanisms in the context of the complexity and heterogeneity in the healthy and diseased mammalian brain complexity and heterogeneity.

**Figures**

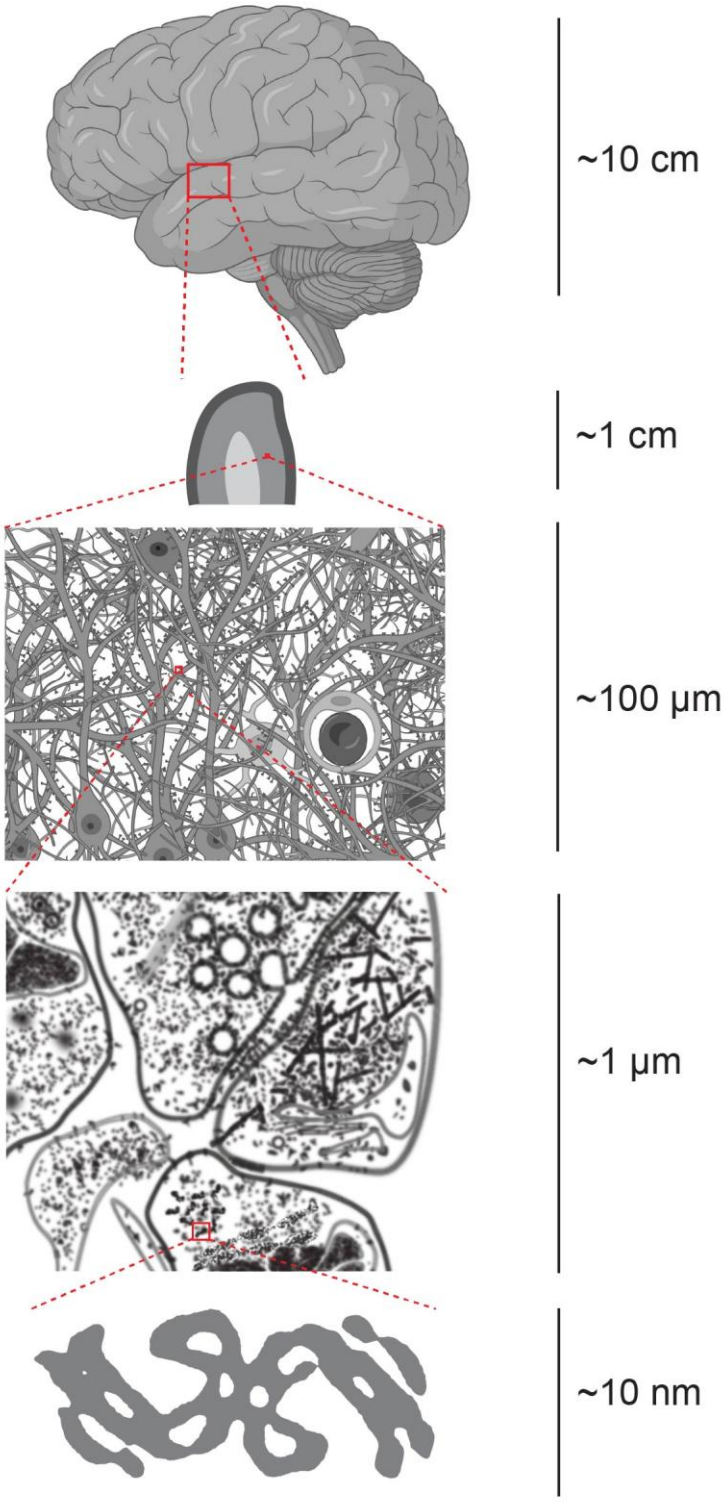


**Figure 1.** Schematic depicting length scales from tissue (cm-mm), to cells (mm-µm), molecular architecture of subcellular compartments (µm-nm), and subnanometer in situ structures. From

top to bottom, human brain, slice through gyrus showing grey and white matter, cellular morphology and heterogeneity, tomographic slice, and subtomogram averaged structure, adapted from [40].

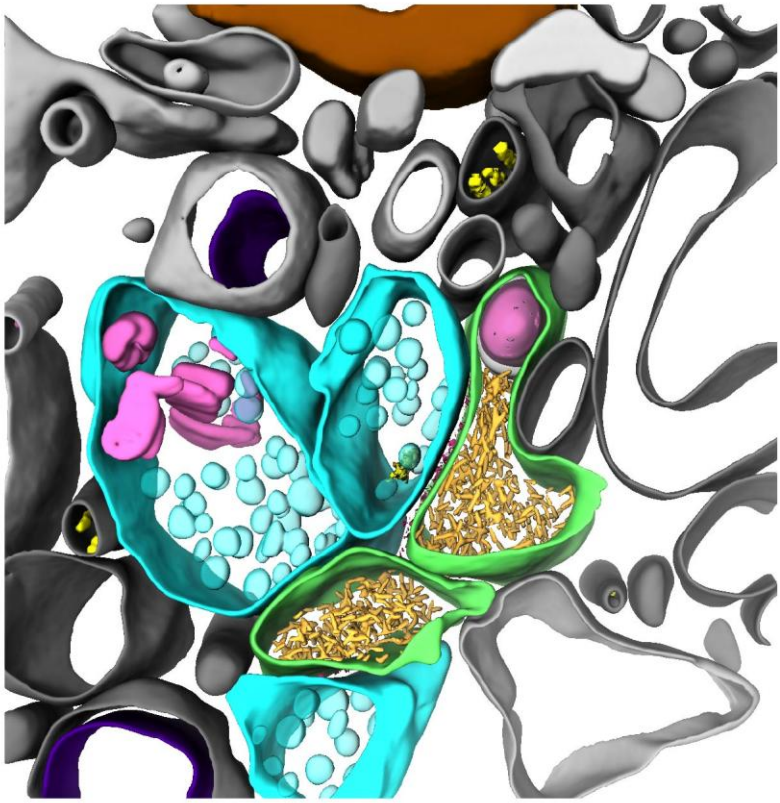

**Figure 2.** An example segmentation of raw tomographic volume showing in-tissue molecular architecture of adult mouse brain synapses, adapted from [62].

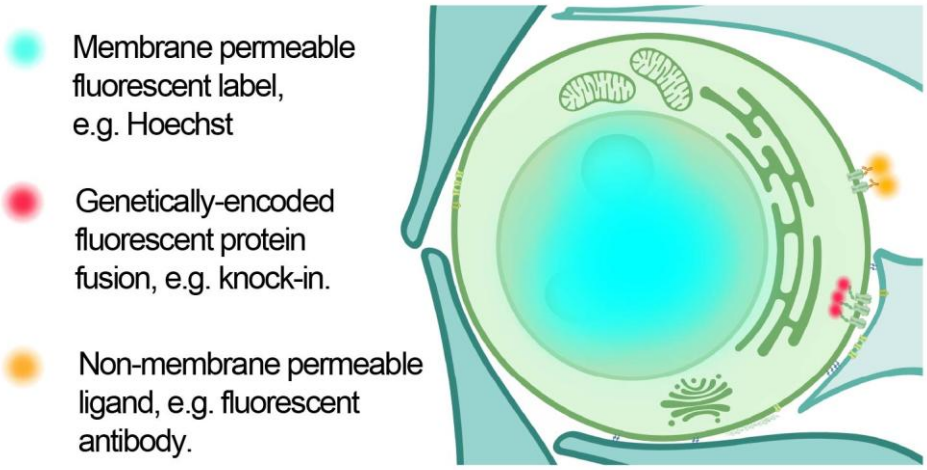


**Figure 3.** Schematic depicting accessibility of fluorescent labels in live imaging experiments using small, membrane permeable ligands (cyan, e.g. Hoechst), genetically encoded in-frame

fluorescent protein tags that can label intracellular targets (red), and non-membrane permeable, fluorescent binders (e.g. fluorescent antibody, orange).

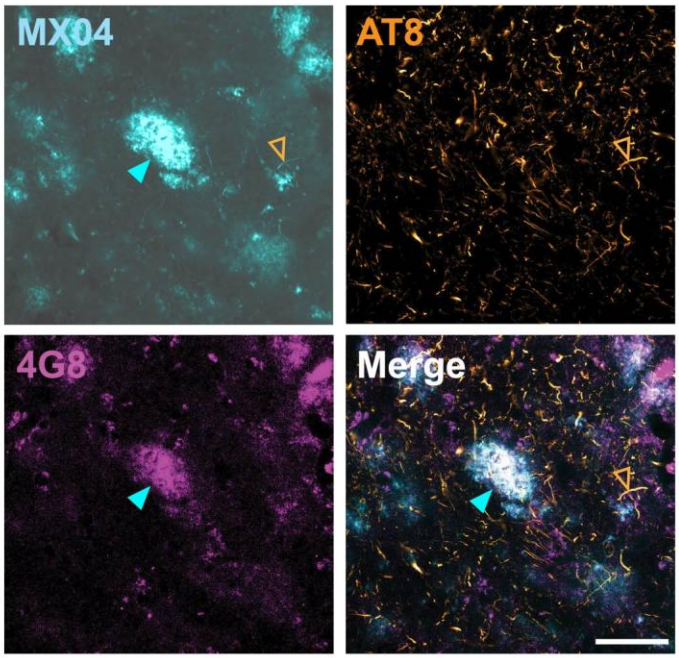


**Figure 4.** Example immunofluorescence images showing validation of the fluorescent ligand methoxy-X04 (MX04) binding to both Aβ (4G8 APP/Aβ monoclonal antibody) and tau (AT8 phospho-tau antibody) deposits in PFA-fixed, post-mortem AD brain tissue. Closed cyan and open orange arrowheads, β-amyloid plaque and tau thread, respectively. Scale bar, 50 µm.

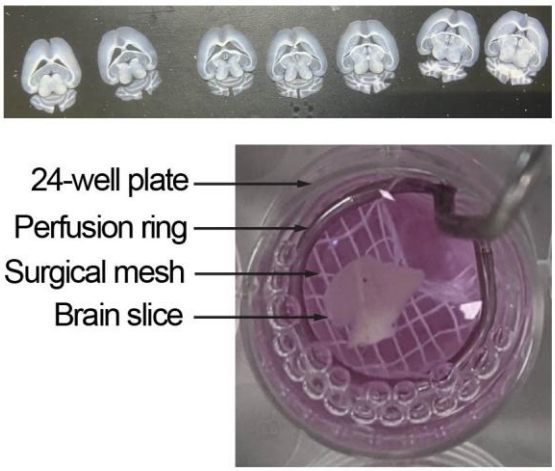


**Figure 5.** Tissue slice preparation and bath application of fluorescent labels. Top, 100 µm thick horizontal, mouse brain acute slices prepared with vibratome. Bottom, 100 µm thick human brain acute slice resting on a surgical mesh within a perfusion chamber.

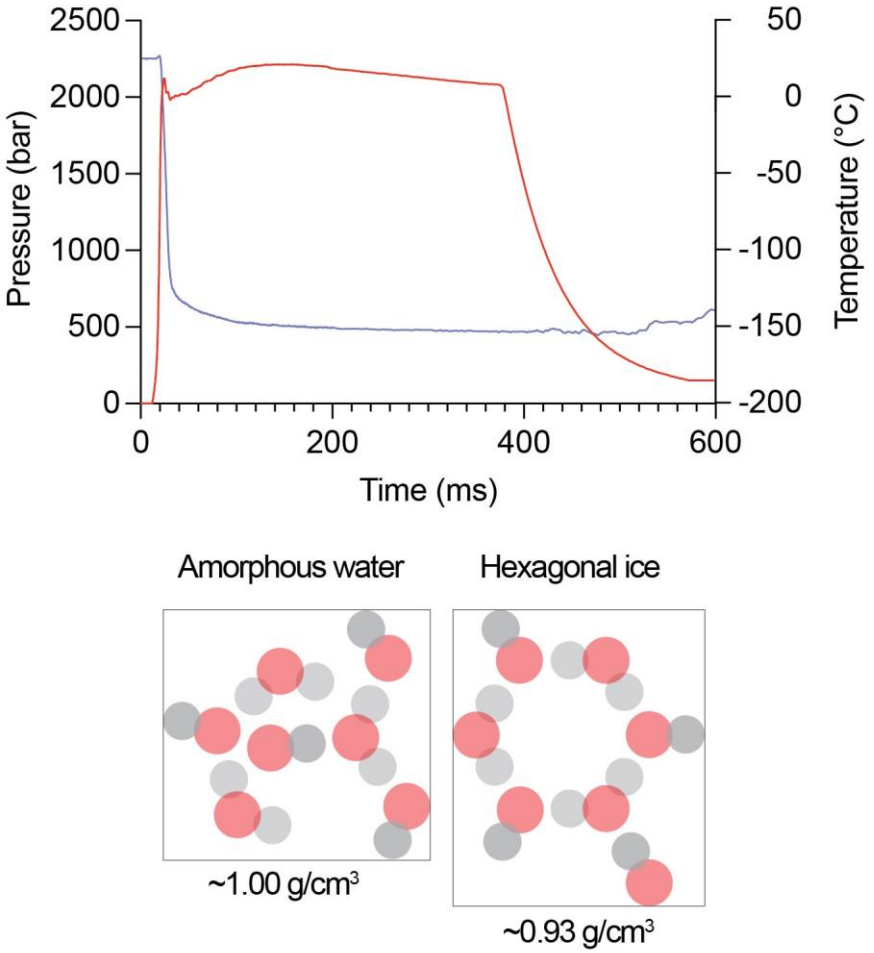


**Figure 6.** Vitrification by high-pressure freezing. Top, graph showing pressure (red curve, left *y*-axis) and temperature (blue, right *y*-axis) profile of tissue specimen during high-pressure freezing. Vitrification is accomplished once the sample temperature falls below ~-150°C, which is typically within ~30 ms. Bottom, schematic showing arrangement of water molecules in amorphous, liquid water and hexagonal ice and approximate density. Oxygen and hydrogen atoms depicted as partially transparent red and grey spheres, respectively.

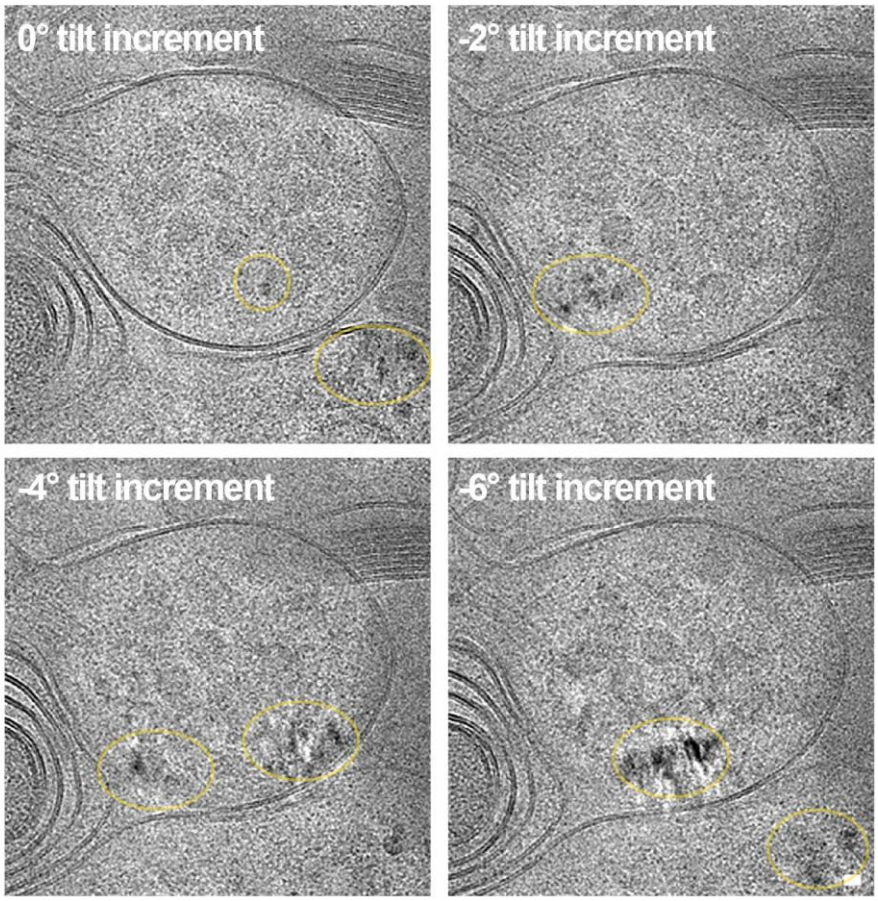


**Figure 7.** Assessing non-vitreous/devitrification in cryoET samples. An example of a non-vitreous/devitrified cryoFIB-SEM liftout lamella of mouse brain is shown. Non-vitreous regions of thinned specimens are easily identified in cryoET tilt series. These show as variations in contrast in one tilt increment that are absent or change in other increments of the tilt series (semi-transparent yellow ellipse). Scale bar, 10 nm.

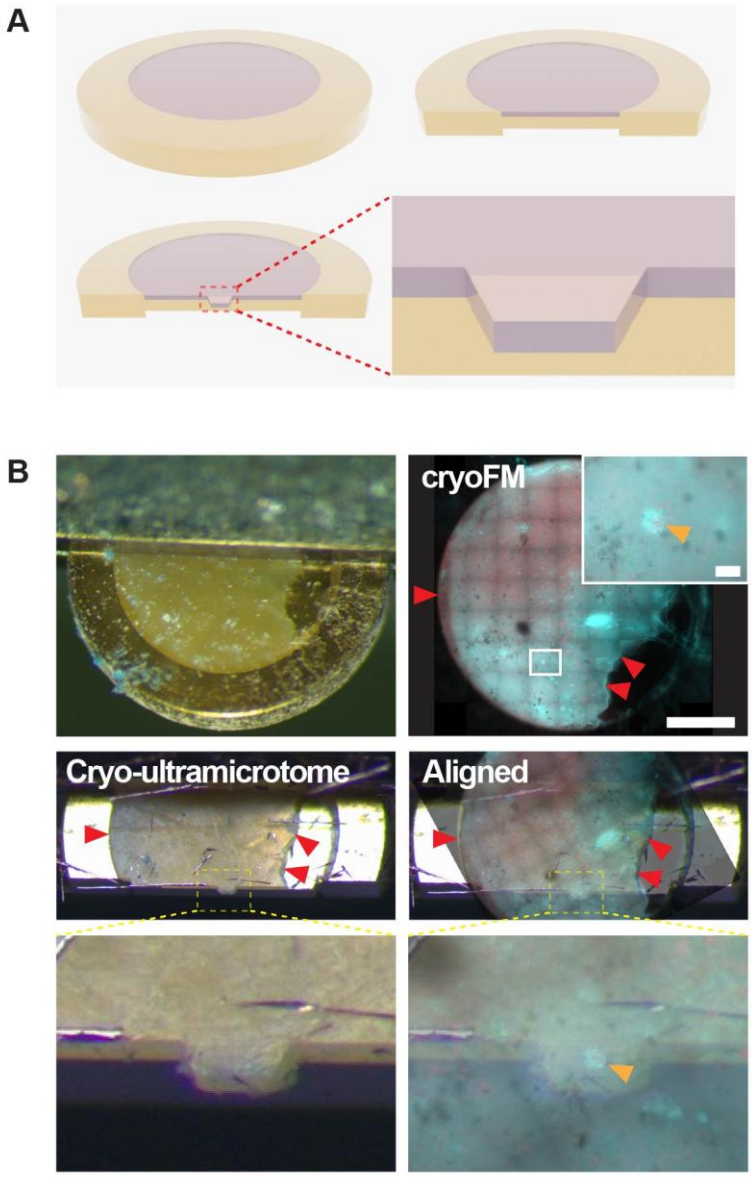


**Figure 8.** CryoCLEM-guided cryo-ultramicrotomy. **A** Schematic showing cryo-ultramicrotomy steps to prepare trapezoid stub of tissue for vitreous cryo-section preparation. Top left and right panels, HPF carrier (gold) containing vitrified tissue (pink) before and after trimming. Bottom left and right, further trimming either side of a target region of tissue leaves a trapezoid stub and closeup, respectively. **B** Example alignment of methoxy-X04 (MX04) cryoFM image of high-pressure frozen (HPF) carrier with stereoscope image in cryo-ultramicrotome. Top left, HPF carrier oriented in sample stage of cryo-ultramicrotome. Top right, cryoFM detecting MX04 (cyan) and autofluorescence (red) with 450/480 nm excitation/emission. Red arrowhead, edge features of tissue used as fiducial markers for alignment. Scale bar, 500 µm. White rectangle, region shown as closeup in inset. Scale bar, 25 µm. Orange arrowhead, target MX04-labelled β-amyloid plaque. Middle left and right, HPF carrier after trimming trapezoid stub of tissue and aligned with cryoFM image to confirm targeting of MX04-labelled β-amyloid, respectively. Dashed yellow rectangles, regions shown as closeup in lower left and right panels.

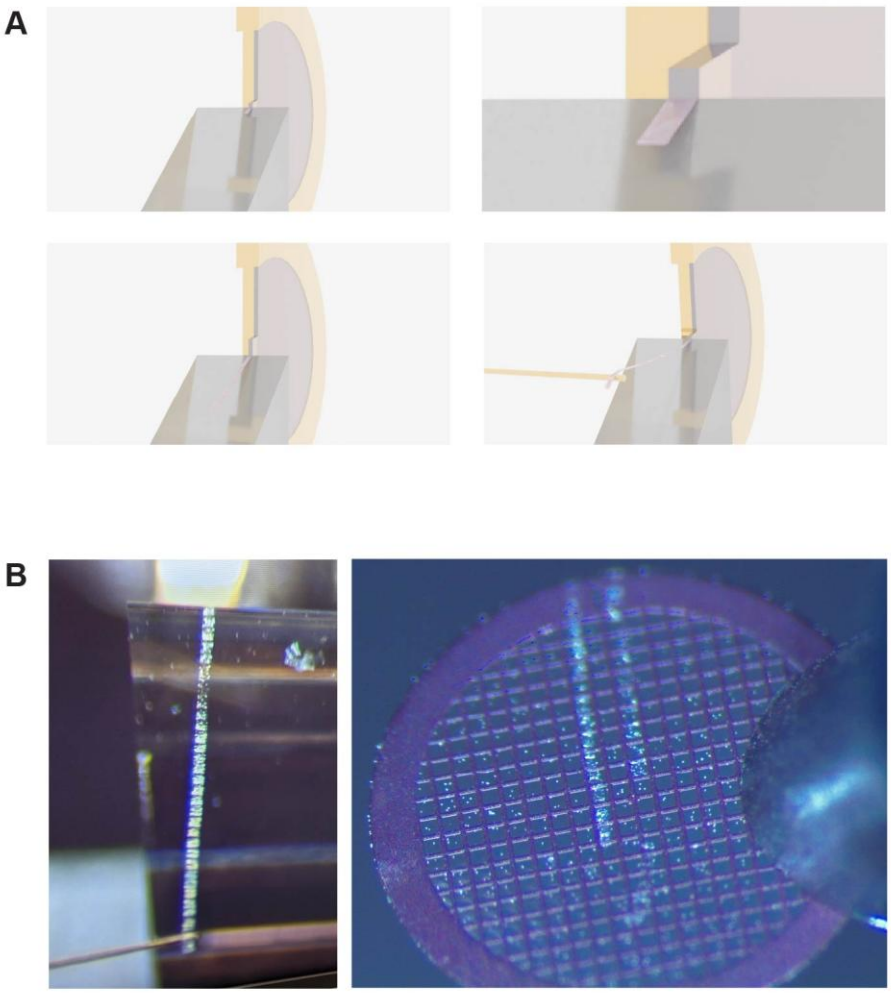


**Figure 9.** Preparation of 100 nm thick vitreous tissue cryo-sections by cryo-ultramicrotomy. **A** Schematic showing steps of cryo-sectioning. Top left and right, diamond knife cutting first section from leading face of trapezoid tissue stub and closeup, respectively. Bottom left and right, showing multiple 100 nm vitreous tissue cryo-sections that adhere to one another forming a tissue ribbon and attached at distal end to gold eyelash controlled by micromanipulators. **B** Left and right, example stereomicroscope image of vitreous tissue cryo-section ribbon attached to gold eyelash and after electrostatic attachment to EM grid, respectively.

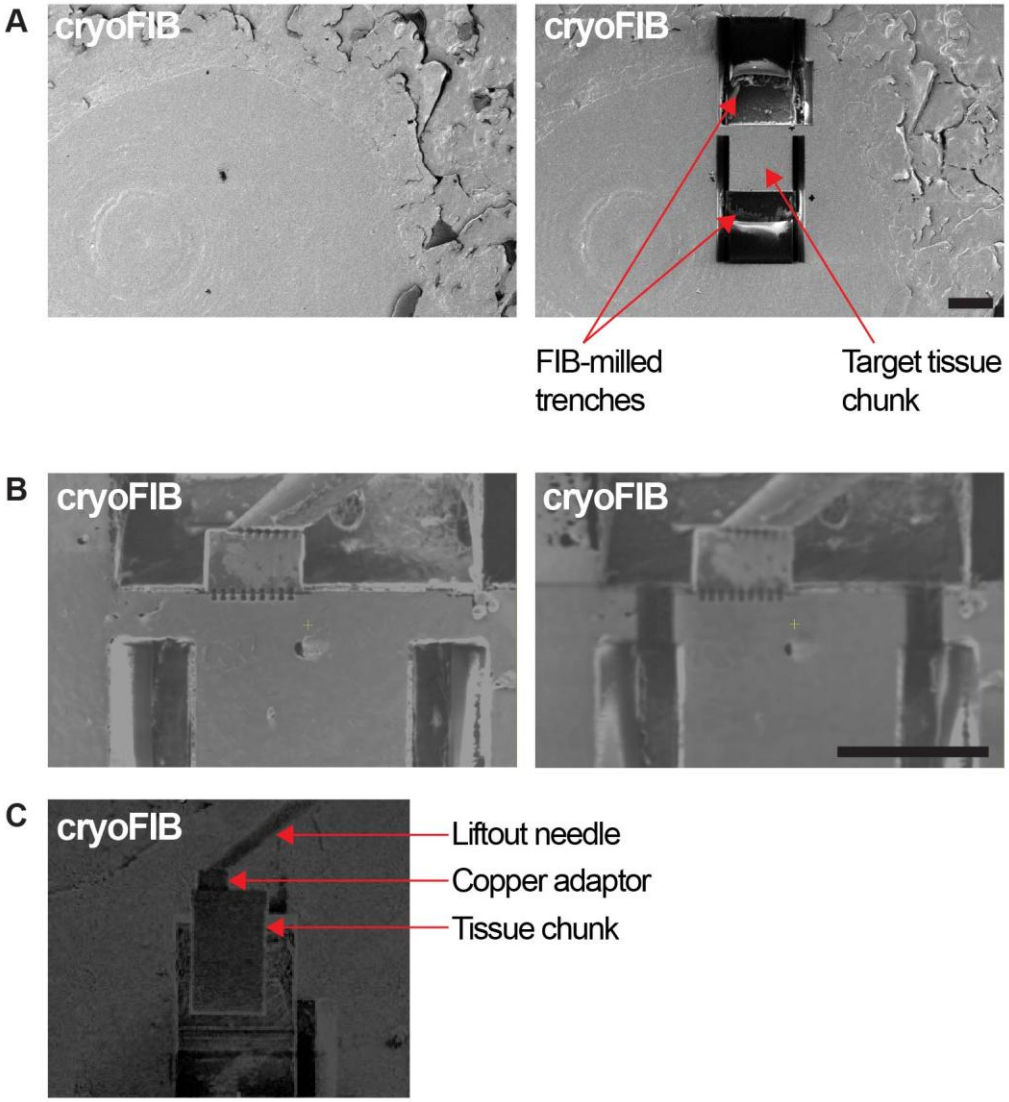


**Figure 10.** Summary of steps in cryoFIB-SEM liftout of HPF vitreous tissue chunk. **A** Left and right, cryo-focused ion beam images of HPF carrier containing vitrified tissue before and after FIB milling trenches (sides and undercut) of target tissue chunk, leaving two points of attachment to surrounding tissue. Scale bar, 50 µm. **B** Left and right, closeup of tissue chunk attached to liftout needle via copper adaptor before and after chunk is released, respectively. Scale bar, 50 µm. **C** Cryo-focused ion beam image of tissue chunk lifted out.

**Figure 11.** Schematic showing cryo-planing the surface of HPF carrier containing vitrified tissue [72]. Left and right, before and after a shallow 'Aztec pyramid'/trapezoid patten is cut into the top surface of the specimen.

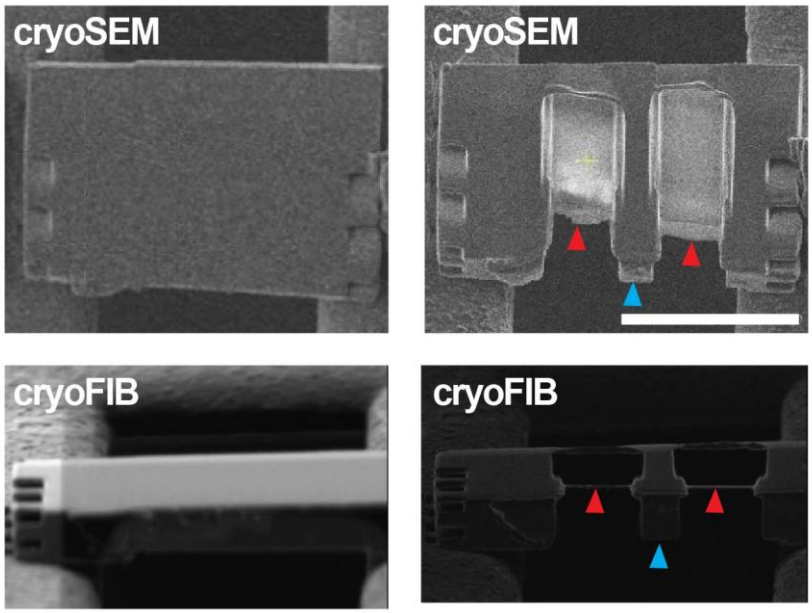


**Figure 12.** CryoFIB-SEM lamella preparation. Left and right panels, liftout tissue chunk adhered to EM grid before and after cryoFIB-milling to generate ~100 nm lamellae, respectively. Top and bottom panels, cryo-scanning EM and cryo-focused ion beam images. Red arrowhead, 100-300 nm cryoFIB-milled lamella. Blue arrowhead, thick regions of tissue chunk left to form a frame and stabilise lamellae. Scale bar, 30 µm.

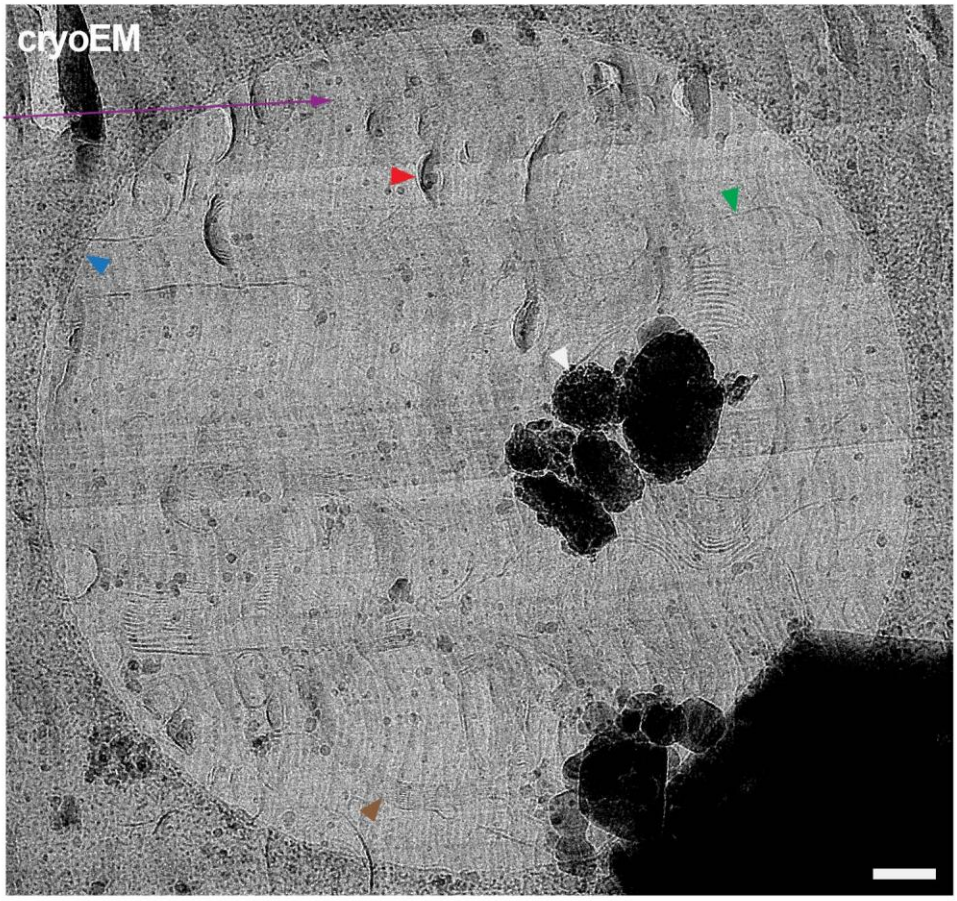


**Figure 13.** Example medium magnification EM image of vitreous cryo-section prepared by cryo-ultramicrotomy with old/blunted diamond knife showing localised damage. Diamond knife imperfections and/or damage cause slight variations in the thickness of the tissue and reveal, purple arrow, the cutting direction. Red arrowhead, localised tear ('crevice') in the vitreous cryo-section. Tissue on right side of tear has been lifted and/or deformed. Blue arrowhead, edge of 3.5 µm holey carbon foil supporting vitreous tissue cryo-section. White arrowhead, ice crystals contaminating the surface of the crystalline ice. Green arrowhead, lipid membrane of subcellular compartment or organelle in tissue. Brown arrowhead, putative myelinated axon. Scale bar, 250 nm.

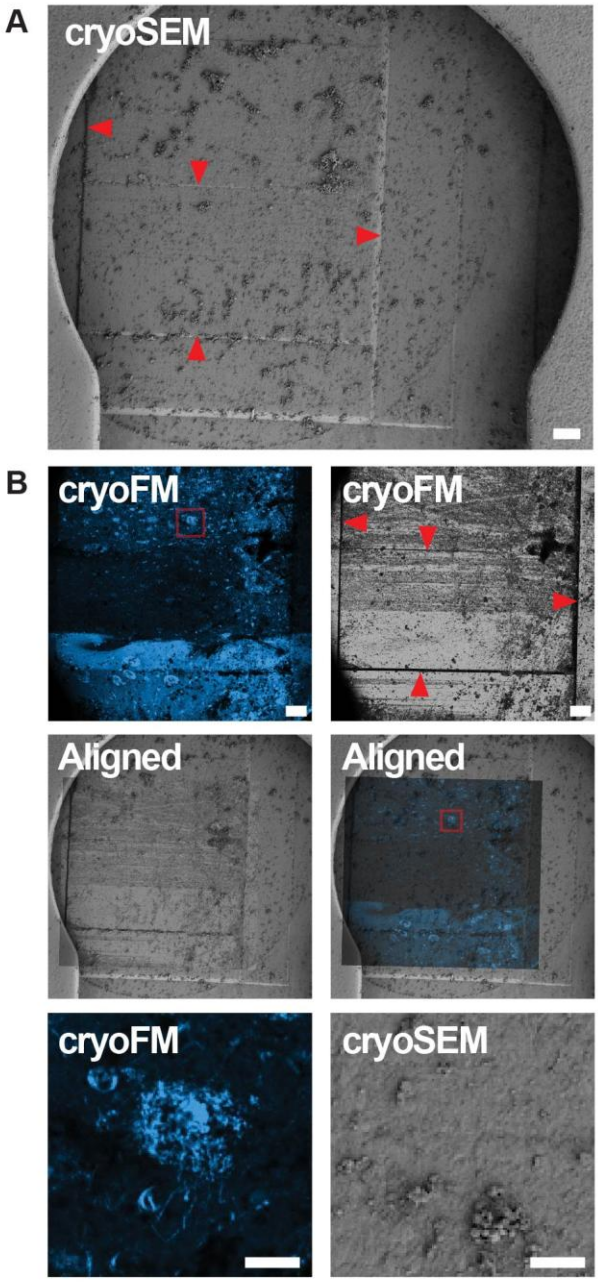


**Figure 14.** Fluorescence-targeted cryoFIB-SEM. **A** CryoSEM image of cryo-planed high-pressure frozen brain tissue. Scale bar, 100 µm. **B** Top left and right, cryo-fluorescence microscopy (cryoFM) image of MX04-labelled amyloid and reflection image of sample surface, respectively. Scale bar, 100 µm. Red arrowheads, fiducial features used for alignment, middle left and right. Red rectangle, MX04-labelled β-amyloid plaque, shown as closeup, bottom left and right, cryoFM and cryoSEM, respectively. Scale bar, 20 µm.

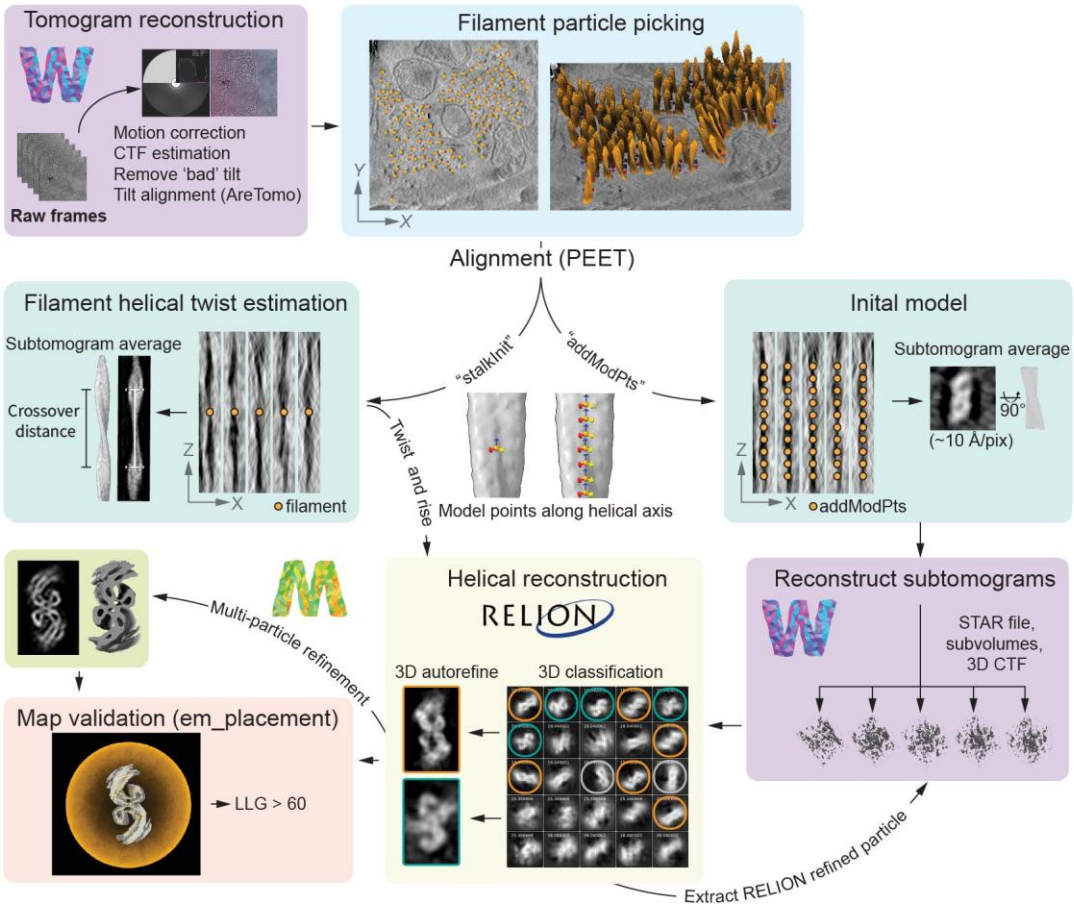


**Figure 15.** A pipeline for in-tissue subtomogram averaging of amyloid. Dose-fractionated tilt-series are pre-processed in Warp (Motion correction, CTF estimation, bad tilt removal)[125,126] and aligned in AreTomo [127]. Filament coordinates are picked from reconstructed tomograms in IMOD [122,209], initially representing the helical axis as a two-point contour. PEET command "stalkInit" is used to estimate the filament centroid, that can be used to average whole filaments and determine filament helical twist [157,158] (used later in RELION). PEET command "addModPts" generates additional model points at user defined intervals along the filament helical axis that can be used to generate an initial model. PEET refined coordinates are extracted as subtomograms in Warp and used as input for helical reconstruction in RELION [168]. Multi-particle refinement in M is used to refine particle poses, accounting for sample geometry and CTF [126]. Final maps are validated with emplace_local, a log-likelihood gain (LLG) score greater than 60 indicates a non-random fit of the model in the map [187,188,210].

**Acknowledgements**

We would like to thank Stephen Meunch and Charlotte Scarff for helpful discussions. RAWF was supported by a UKRI Future Leader Fellowship (MR/V022644/1), UKRI MRC project grant (UKRI1449) and the Cure Alzheimer's Fund.

**References**

[1] Siletti K, Hodge R, Albiach AM, Lee KW, Ding S-L, Hu L, Lönnerberg P, Bakken T, Casper T, Clark M, Dee N, Gloe J, Hirschstein D, Shapovalova NV, Keene CD, Nyhus J, Tung H, Yanny AM, Arenas E, Lein ES, Linnarsson S. Transcriptomic diversity of cell types across the adult human brain. Science 2023;382:eadd7046. https://doi.org/10.1126/science.add7046.

[2] Herculano-Houzel S. The Human Brain in Numbers: A Linearly Scaled-up Primate Brain. Front Hum Neurosci 2009;3:31. https://doi.org/10.3389/neuro.09.031.2009.

[3] Sammons M, Popescu MC, Chi J, Liberles SD, Gogolla N, Rolls A. Brain-body physiology: Local, reflex, and central communication. Cell 2024;187:5877–90. https://doi.org/10.1016/j.cell.2024.08.050.

[4] Feigin VL, Nichols E, Alam T, Bannick MS, Beghi E, Blake N, Culpepper WJ, Dorsey ER, Elbaz A, Ellenbogen RG, Fisher JL, Fitzmaurice C, Giussani G, Glennie L, James SL, Johnson CO, Kassebaum NJ, Logroscino G, Marin B, Mountjoy-Venning WC, Nguyen M, Ofori-Asenso R, Patel AP, Piccininni M, Roth GA, Steiner TJ, Stovner LJ, Szoeke CEI, Theadom A, Vollset SE, Wallin MT, Wright C, Zunt JR, Abbasi N, Abd-Allah F, Abdelalim A, Abdollahpour I, Aboyans V, Abraha HN, Acharya D, Adamu AA, Adebayo OM, Adeoye AM, Adsuar JC, Afarideh M, Agrawal S, Ahmadi A, Ahmed MB, Aichour AN, Aichour I, Aichour MTE, Akinyemi RO, Akseer N, Al-Eyadhy A, Salman RA-S, Alahdab F, Alene KA, Aljunid SM, Altirkawi K, Alvis-Guzman N, Anber NH, Antonio CAT, Arabloo J, Aremu O, Ärnlöv J, Asayesh H, Asghar RJ, Atalay HT, Awasthi A, Quintanilla BPA, Ayuk TB, Badawi A, Banach M, Banoub JAM, Barboza MA, Barker-Collo SL, Bärnighausen TW, Baune BT, Bedi N, Behzadifar M, Behzadifar M, Béjot Y, Bekele BB, Belachew AB, Bennett DA, Bensenor IM, Berhane A, Beuran M, Bhattacharyya K, Bhutta ZA, Biadgo B, Bijani A, Bililign N, Sayeed MSB, Blazes CK, Brayne C, Butt ZA, Campos-Nonato IR, Cantu-Brito C, Car M, Cárdenas R, Carrero JJ, Carvalho F, Castañeda-Orjuela CA, Castro F, Catalá-López F, Cerin E, Chaiah Y, Chang J-C, Chatziralli I, Chiang PP-C, Christensen H, Christopher DJ, Cooper C, Cortesi PA, Costa VM, Criqui MH, Crowe CS, Damasceno AAM, Daryani A, Cruz-Góngora VD la, Hoz FPD la, Leo DD, Demoz GT, Deribe K, Dharmaratne SD, Diaz D, Dinberu MT, Djalalinia S, Doku DT, Dubey M, Dubljanin E, Duken EE, Edvardsson D, El-Khatib Z, Endres M, Endries AY, Eskandarieh S, Esteghamati A, Esteghamati S, Farhadi F, Faro A, Farzadfar F, Farzaei MH, Fatima B, Fereshtehnejad S-M, Fernandes E, Feyissa GT, Filip I, Fischer F, Fukumoto T, Ganji M, Gankpe FG, Garcia-Gordillo MA, Gebre AK, Gebremichael TG, Gelaw BK, Geleijnse JM, Geremew D, Gezae KE, Ghasemi-Kasman M, Gidey MY, Gill PS, Gill TK, Girma ET, Gnedovskaya EV, Goulart AC, Grada A, Grosso G, Guo Y, Gupta R, Gupta R, Haagsma JA, Hagos TB, Haj-Mirzaian A, Haj-Mirzaian A, Hamadeh RR, Hamidi S, Hankey GJ, Hao Y, Haro JM, Hassankhani H, Hassen HY, Havmoeller R, Hay SI, Hegazy MI, Heidari B, Henok A, Heydarpour F, Hoang CL, Hole MK, Rad EH, Hosseini SM, Hu G, Igumbor EU, Ilesanmi OS, Irvani SSN, Islam SMS, Jakovljevic M, Javanbakht M, Jha RP, Jobanputra YB, Jonas JB, Jozwiak JJ, Jürisson M,

Kahsay A, Kalani R, Kalkonde Y, Kamil TA, Kanchan T, Karami M, Karch A, Karimi N, Kasaeian A, Kassa TD, Kassa ZY, Kaul A, Kefale AT, Keiyoro PN, Khader YS, Khafaie MA, Khalil IA, Khan EA, Khang Y-H, Khazaie H, Kiadaliri AA, Kiirithio DN, Kim AS, Kim D, Kim Y-E, Kim YJ, Kisa A, Kokubo Y, Koyanagi A, Krishnamurthi RV, Defo BK, Bicer BK, Kumar M, Lacey B, Lafranconi A, Lansingh VC, Latifi A, Leshargie CT, Li S, Liao Y, Linn S, Lo WD, Lopez JCF, Lorkowski S, Lotufo PA, Lucas RM, Lunevicius R, Mackay MT, Mahotra NB, Majdan M, Majdzadeh R, Majeed A, Malekzadeh R, Malta DC, Manafi N, Mansournia MA, Mantovani LG, März W, Mashamba-Thompson TP, Massenburg BB, Mate KKV, McAlinden C, McGrath JJ, Mehta V, Meier T, Meles HG, Melese A, Memiah PTN, Memish ZA, Mendoza W, Mengistu DT, Mengistu G, Meretoja A, Meretoja TJ, Mestrovic T, Miazgowski B, Miazgowski T, Miller TR, Mini G, Mirrakhimov EM, Moazen B, Mohajer B, Mezerji NMG, Mohammadi M, Mohammadi-Khanaposhtani M, Mohammadibakhsh R, Mohammadnia-Afrouzi M, Mohammed S, Mohebi F, Mokdad AH, Monasta L, Mondello S, Moodley Y, Moosazadeh M, Moradi G, Moradi-Lakeh M, Moradinazar M, Moraga P, Velásquez IM, Morrison SD, Mousavi SM, Muhammed OS, Muruet W, Musa KI, Mustafa G, Naderi M, Nagel G, Naheed A, Naik G, Najafi F, Nangia V, Negoi I, Negoi RI, Newton CRJ, Ngunjiri JW, Nguyen CT, Nguyen LH, Ningrum DNA, Nirayo YL, Nixon MR, Norrving B, Noubiap JJ, Shiadeh MN, Nyasulu PS, Ogah OS, Oh I-H, Olagunju AT, Olagunju TO, Olivares PR, Onwujekwe OE, Oren E, Owolabi MO, PA M, Pakpour AH, Pan W-H, Panda-Jonas S, Pandian JD, Patel SK, Pereira DM, Petzold M, Pillay JD, Piradov MA, Polanczyk GV, Polinder S, Postma MJ, Poulton R, Poustchi H, Prakash S, Prakash V, Qorbani M, Radfar A, Rafay A, Rafiei A, Rahim F, Rahimi-Movaghar V, Rahman M, Rahman MHU, Rahman MA, Rajati F, Ram U, Ranta A, Rawaf DL, Rawaf S, Reinig N, Reis C, Renzaho AMN, Resnikoff S, Rezaeian S, Rezai MS, González CMR, Roberts NLS, Roever L, Ronfani L, Roro EM, Roshandel G, Rostami A, Sabbagh P, Sacco RL, Sachdev PS, Saddik B, Safari H, Safari-Faramani R, Safi S, Safiri S, Sagar R, Sahathevan R, Sahebkar A, Sahraian MA, Salamati P, Zahabi SS, Salimi Y, Samy AM, Sanabria J, Santos IS, Milicevic MMS, Sarrafzadegan N, Sartorius B, Sarvi S, Sathian B, Satpathy M, Sawant AR, Sawhney M, Schneider IJC, Schöttker B, Schwebel DC, Seedat S, Sepanlou SG, Shabaninejad H, Shafieesabet A, Shaikh MA, Shakir RA, Shams-Beyranvand M, Shamsizadeh M, Sharif M, Sharif-Alhoseini M, She J, Sheikh A, Sheth KN, Shigematsu M, Shiri R, Shirkoohi R, Shiue I, Siabani S, Siddiqi TJ, Sigfusdottir ID, Sigurvinsdottir R, Silberberg DH, Silva JP, Silveira DGA, Singh JA, Sinha DN, Skiadaresi E, Smith M, Sobaih BH, Sobhani S, Soofi M, Soyiri IN, Sposato LA, Stein DJ, Stein MB, Stokes MA, Sufiyan MB, Sykes BL, Sylaja P, Tabarés-Seisdedos R, Ao BJT, Tehrani-Banihashemi A, Temsah M-H, Temsah O, Thakur JS, Thrift AG, Topor-Madry R, Tortajada-Girbés M, Tovani-Palone MR, Tran BX, Tran KB, Truelsen TC, Tsadik AG, Car LT, Ukwaja KN, Ullah I, Usman MS, Uthman OA, Valdez PR, Vasankari TJ, Vasanthan R, Veisani Y, Venketasubramanian N, Violante FS, Vlassov V, Vosoughi K, Vu GT, Vujcic IS, Wagnew FS, Waheed Y, Wang Y-P, Weiderpass E, Weiss J, Whiteford HA, Wijeratne T, Winkler AS, Wiysonge CS, Wolfe CDA, Xu G, Yadollahpour A, Yamada T, Yano Y, Yaseri M, Yatsuya H, Yimer EM, Yip P, Yisma E, Yonemoto N, Yousefifard M, Yu C, Zaidi Z, Zaman SB, Zamani M, Zandian H, Zare Z, Zhang Y, Zodpey S, Naghavi M, Murray CJL, Vos T. Global, regional, and national burden of neurological disorders, 1990–2016: a systematic analysis for the Global Burden of Disease Study 2016. Lancet Neurol 2019;18:459–80. https://doi.org/10.1016/s1474-4422(18)30499-x.

[5] Long JM, Holtzman DM. Alzheimer Disease: An Update on Pathobiology and Treatment Strategies. Cell 2019;179:312–39. https://doi.org/10.1016/j.cell.2019.09.001.

[6] Wilson DM, Cookson MR, Bosch LVD, Zetterberg H, Holtzman DM, Dewachter I. Hallmarks of neurodegenerative diseases. Cell 2023;186:693–714. https://doi.org/10.1016/j.cell.2022.12.032.

[7] Hardy J, Escott-Price V. The genetics of neurodegenerative diseases is the genetics of age-related damage clearance failure. Mol Psychiatry 2025;30:2748–53. https://doi.org/10.1038/s41380-025-02911-7.

[8] Goate A, Chartier-Harlin M-C, Mullan M, Brown J, Crawford F, Fidani L, Giuffra L, Haynes A, Irving N, James L, Mant R, Newton P, Rooke K, Roques P, Talbot C, Pericak-Vance M, Roses A, Williamson R, Rossor M, Owen M, Hardy J. Segregation of a missense mutation in the amyloid precursor protein gene with familial Alzheimer's disease. Nature 1991;349:704–6. https://doi.org/10.1038/349704a0.

[9] Poorkaj P, Bird TD, Wijsman E, Nemens E, Garruto RM, Anderson L, Andreadis A, Wiederholt WC, Raskind M, Schellenberg GD. Tau is a candidate gene for chromosome 17 frontotemporal dementia. Ann Neurol 1998;43:815–25. https://doi.org/10.1002/ana.410430617.

[10] Hutton M, Lendon CL, Rizzu P, Baker M, Froelich S, Houlden H, Pickering-Brown S, Chakraverty S, Isaacs A, Grover A, Hackett J, Adamson J, Lincoln S, Dickson D, Davies P, Petersen RC, Stevens M, Graaff E de, Wauters E, Baren J van, Hillebrand M, Joosse M, Kwon JM, Nowotny P, Che LK, Norton J, Morris JC, Reed LA, Trojanowski J, Basun H, Lannfelt L, Neystat M, Fahn S, Dark F, Tannenberg T, Dodd PR, Hayward N, Kwok JBJ, Schofield PR, Andreadis A, Snowden J, Craufurd D, Neary D, Owen F, Oostra BA, Hardy J, Goate A, Swieten J van, Mann D, Lynch T, Heutink P. Association of missense and 5′-splice-site mutations in tau with the inherited dementia FTDP-17. Nature 1998;393:702–5. https://doi.org/10.1038/31508.

[11] Spillantini MG, Murrell JR, Goedert M, Farlow MR, Klug A, Ghetti B. Mutation in the tau gene in familial multiple system tauopathy with presenile dementia. Proc Natl Acad Sci 1998;95:7737–41. https://doi.org/10.1073/pnas.95.13.7737.

[12] Polymeropoulos MH, Lavedan C, Leroy E, Ide SE, Dehejia A, Dutra A, Pike B, Root H, Rubenstein J, Boyer R, Stenroos ES, Chandrasekharappa S, Athanassiadou A, Papapetropoulos T, Johnson WG, Lazzarini AM, Duvoisin RC, Iorio GD, Golbe LI, Nussbaum RL. Mutation in the α-Synuclein Gene Identified in Families with Parkinson's Disease. Science 1997;276:2045–7. https://doi.org/10.1126/science.276.5321.2045.

[13] Lee WJ, Brown JA, Kim HR, Joie RL, Cho H, Lyoo CH, Rabinovici GD, Seong J-K, Seeley WW, Initiative ADN. Regional Aβ-tau interactions promote onset and acceleration of Alzheimer's disease tau spreading. Neuron 2022;110:1932-1943.e5. https://doi.org/10.1016/j.neuron.2022.03.034.

[14] Goedert M. Alzheimer's and Parkinson's diseases: The prion concept in relation to assembled Aβ, tau, and α-synuclein. Science 2015;349:1255555. https://doi.org/10.1126/science.1255555.

[15] Dyck CH van, Swanson CJ, Aisen P, Bateman RJ, Chen C, Gee M, Kanekiyo M, Li D, Reyderman L, Cohen S, Froelich L, Katayama S, Sabbagh M, Vellas B, Watson D, Dhadda

S, Irizarry M, Kramer LD, Iwatsubo T. Lecanemab in Early Alzheimer's Disease. N Engl J Med 2022;388:9–21. https://doi.org/10.1056/nejmoa2212948.

[16] Sims JR, Zimmer JA, Evans CD, Lu M, Ardayfio P, Sparks J, Wessels AM, Shcherbinin S, Wang H, Nery ESM, Collins EC, Solomon P, Salloway S, Apostolova LG, Hansson O, Ritchie C, Brooks DA, Mintun M, Skovronsky DM, Investigators T-A 2, Abreu R, Agarwal P, Aggarwal P, Agronin M, Allen A, Altamirano D, Alva G, Andersen J, Anderson A, Anderson D, Arnold J, Asada T, Aso Y, Atit V, Ayala R, Badruddoja M, Badzio-jagiello H, Bajacek M, Barton D, Bear D, Benjamin S, Bergeron R, Bhatia P, Black S, Block A, Bolouri M, Bond W, Bouthillier J, Brangman S, Brew B, Brisbin S, Brisken T, Brodtmann A, Brody M, Brosch J, Brown C, Brownstone P, Bukowczan S, Burns J, Cabrera A, Capote H, Carrasco A, Yepez JC, Chavez E, Chertkow H, Chyrchel-paszkiewicz U, Ciabarra A, Clemmons E, Cohen D, Cohen R, Cohen I, Concha M, Costell B, Crimmins D, Cruz-pagan Y, Cueli A, Cupelo R, Czarnecki M, Darby D, Dautzenberg P l j, Deyn PD, Gandara JDL, Deck K, Dibenedetto D, Dibuono M, Dinnerstein E, Dirican A, Dixit S, Dobryniewski J, Drake R, Drysdale P, Duara R, Duffy J, Ellenbogen A, Faradji V, Feinberg M, Feldman R, Fishman S, Flitman S, Forchetti C, Fraga I, Frank A, Frishberg B, Fujigasaki H, Fukase H, Fumero I, Furihata K, Galloway C, Gandhi R, George K, Germain M, Gitelman D, Goetsch N, Goldfarb D, Goldstein M, Goldstick L, Rojas YG, Goodman I, Greeley D, Griffin C, Grigsby E, Grosz D, Hafner K, Hart D, Henein S, Herskowitz B, Higashi S, Higashi Y, Ho G, Hodgson J, Hohenberg M, Hollenbeck L, Holub R, Hori T, Hort J, Ilkowski J, Ingram KJ, Isaac M, Ishikawa M, Janu L, Johnston M, Julio W, Justiz W, Kaga T, Kakigi T, Kalafer M, Kamijo M, Kaplan J, Karathanos M, Katayama S, Kaul S, Keegan A, Kerwin D, Khan U, Khan A, Kimura N, Kirk G, Klodowska G, Kowa H, Kutz C, Kwentus J, Lai R, Lall A, Lawrence M, Lee E, Leon R, Linker G, Lisewski P, Liss J, Liu C, Losk S, Lukaszyk E, Lynch J, Macfarlane S, Macsweeney J, Mannering N, Markovic O, Marks D, Masdeu J, Matsui Y, Matsuishi K, Mcallister P, Mcconnehey B, Mcelveen A, Mcgill L, Mecca A, Mega M, Mensah J, Mickielewicz A, Minaeian A, Mocherla B, Murphy C, Murphy P, Nagashima H, Nair A, Nair M, Nardandrea J, Nash M, Nasreddine Z, Nishida Y, Norton J, Nunez L, Ochiai J, Ohkubo T, Okamura Y, Okorie E, Olivera E, O'mahony J, Omidvar O, Ortiz-Cruz D, Osowa A, Papka M, Parker A, Patel P, Patel A, Patel M, Patry C, Peckham E, Pfeffer M, Pietras A, Plopper M, Porsteinsson A, Robitaille RP, Prins N, Puente O, Ratajczak M, Rhee M, Ritter A, Rodriguez R, Ables LR, Rojas J, Ross J, Royer P, Rubin J, Russell D, Rutgers SM, Rutrick S, Sadowski M, Safirstein B, Sagisaka T, Scharre D, Schneider L, Schreiber C, Schrift M, Schulz P, Schwartz H, Schwartzbard J, Scott J, Selem L, Sethi P, Sha S, Sharlin K, Sharma S, Shiovitz T, Shiwach R, Sladek M, Sloan B, Smith A, Solomon P, Sorial E, Sosa E, Stedman M, Steen S, Stein L, Stolyar A, Stoukides J, Sudoh S, Sutton J, Syed J, Szigeti K, Tachibana H, Takahashi Y, Tateno A, Taylor JD, Taylor K, Tcheremissine O, Thebaud A, Thein S, Thurman L, Toenjes S, Toji H, Toma M, Tran D, Trueba P, Tsujimoto M, Turner R, Uchiyama A, Ussorowska D, Vaishnavi S, Valor E, Vandersluis J, Vasquez A, Velez J, Verghese C, Vodickova-borzova K, Watson D, Weidman D, Weisman D, White A, Willingham K, Winkel I, Winner P, Winston J, Wolff A, Yagi H, Yamamoto H, Yathiraj S, Yoshiyama Y, Zboch M. Donanemab in Early Symptomatic Alzheimer Disease. JAMA 2023;330:512–27. https://doi.org/10.1001/jama.2023.13239.

[17] Cohen AS, Calkins E. Electron Microscopic Observations on a Fibrous Component in Amyloid of Diverse Origins. Nature 1959;183:1202–3. https://doi.org/10.1038/1831202a0.

[18] Eanes ED, Glenner GG. X-ray diffraction studies on amyloid filaments. J Histochem Cytochem 1968;16:673–7. https://doi.org/10.1177/16.11.673.

[19] Sunde M, Serpell LC, Bartlam M, Fraser PE, Pepys MB, Blake CCF. Common core structure of amyloid fibrils by synchrotron X-ray diffraction11Edited by F. E. Cohen. J Mol Biol 1997;273:729–39. https://doi.org/10.1006/jmbi.1997.1348.

[20] Nelson R, Sawaya MR, Balbirnie M, Madsen AØ, Riekel C, Grothe R, Eisenberg D. Structure of the cross-β spine of amyloid-like fibrils. Nature 2005;435:773–8. https://doi.org/10.1038/nature03680.

[21] Eisenberg DS, Sawaya MR. Structural Studies of Amyloid Proteins at the Molecular Level. Annu Rev Biochem 2017;86:69–95. https://doi.org/10.1146/annurev-biochem-061516-045104.

[22] Lu J-X, Qiang W, Yau W-M, Schwieters CD, Meredith SC, Tycko R. Molecular Structure of β-Amyloid Fibrils in Alzheimer's Disease Brain Tissue. Cell 2013;154:1257–68.

[23] Guerrero-Ferreira R, Taylor NM, Mona D, Ringler P, Lauer ME, Riek R, Britschgi M, Stahlberg H. Cryo-EM structure of alpha-synuclein fibrils. eLife 2018;7:e36402. https://doi.org/10.7554/elife.36402.

[24] Gremer L, Schölzel D, Schenk C, Reinartz E, Labahn J, Ravelli RBG, Tusche M, Lopez-Iglesias C, Hoyer W, Heise H, Willbold D, Schröder GF. Fibril structure of amyloid-β(1–42) by cryo–electron microscopy. Science 2017;358:116–9. https://doi.org/10.1126/science.aao2825.

[25] Scheres SHW, Ryskeldi-Falcon B, Goedert M. Molecular pathology of neurodegenerative diseases by cryo-EM of amyloids. Nature 2023;621:701–10. https://doi.org/10.1038/s41586-023-06437-2.

[26] Fitzpatrick AWP, Falcon B, He S, Murzin AG, Murshudov G, Garringer HJ, Crowther RA, Ghetti B, Goedert M, Scheres SHW. Cryo-EM structures of tau filaments from Alzheimer's disease. Nature 2017;547:185–90. https://doi.org/10.1038/nature23002.

[27] Zhang W, Tarutani A, Newell KL, Murzin AG, Matsubara T, Falcon B, Vidal R, Garringer HJ, Shi Y, Ikeuchi T, Murayama S, Ghetti B, Hasegawa M, Goedert M, Scheres SHW. Novel tau filament fold in corticobasal degeneration. Nature 2020;580:283–7. https://doi.org/10.1038/s41586-020-2043-0.

[28] Falcon B, Zhang W, Schweighauser M, Murzin AG, Vidal R, Garringer HJ, Ghetti B, Scheres SHW, Goedert M. Tau filaments from multiple cases of sporadic and inherited Alzheimer's disease adopt a common fold. Acta Neuropathol 2018;136:699–708. https://doi.org/10.1007/s00401-018-1914-z.

[29] Falcon B, Zivanov J, Zhang W, Murzin AG, Garringer HJ, Vidal R, Crowther RA, Newell KL, Ghetti B, Goedert M, Scheres SHW. Novel tau filament fold in chronic traumatic encephalopathy encloses hydrophobic molecules. Nature 2019;568:420–3. https://doi.org/10.1038/s41586-019-1026-5.

[30] Falcon B, Zhang W, Murzin AG, Murshudov G, Garringer HJ, Vidal R, Crowther RA, Ghetti B, Scheres SHW, Goedert M. Structures of filaments from Pick's disease reveal a novel tau protein fold. Nature 2018;561:137–40. https://doi.org/10.1038/s41586-018-0454-y.

[31] Shi Y, Murzin AG, Falcon B, Epstein A, Machin J, Tempest P, Newell KL, Vidal R, Garringer HJ, Sahara N, Higuchi M, Ghetti B, Jang M-K, Scheres SHW, Goedert M. Cryo-EM structures of tau filaments from Alzheimer's disease with PET ligand APN-1607. Acta Neuropathol 2021;141:697–708. https://doi.org/10.1007/s00401-021-02294-3.

[32] Lövestam S, Koh FA, Knippenberg B van, Kotecha A, Murzin AG, Goedert M, Scheres SH. Assembly of recombinant tau into filaments identical to those of Alzheimer's disease and chronic traumatic encephalopathy. Elife 2022;11:e76494. https://doi.org/10.7554/elife.76494.

[33] Lövestam S, Li D, Wagstaff JL, Kotecha A, Kimanius D, McLaughlin SH, Murzin AG, Freund SMV, Goedert M, Scheres SHW. Disease-specific tau filaments assemble via polymorphic intermediates. Nature 2024;625:119–25. https://doi.org/10.1038/s41586-023-06788-w.

[34] Yang Y, Arseni D, Zhang W, Huang M, Lövestam S, Schweighauser M, Kotecha A, Murzin AG, Peak-Chew SY, Macdonald J, Lavenir I, Garringer HJ, Gelpi E, Newell KL, Kovacs GG, Vidal R, Ghetti B, Ryskeldi-Falcon B, Scheres SHW, Goedert M. Cryo-EM structures of amyloid-β 42 filaments from human brains. Science 2022;375:167–72. https://doi.org/10.1126/science.abm7285.

[35] Zielinski M, Reyes FSP, Gremer L, Schemmert S, Frieg B, Schäfer LU, Willuweit A, Donner L, Elvers M, Nilsson LNG, Syvänen S, Sehlin D, Ingelsson M, Willbold D, Schröder GF. Cryo-EM of Aβ fibrils from mouse models find tg-APPArcSwe fibrils resemble those found in patients with sporadic Alzheimer's disease. Nat Neurosci 2023;26:2073–80. https://doi.org/10.1038/s41593-023-01484-4.

[36] Yang Y, Murzin AG, Peak-Chew S, Franco C, Garringer HJ, Newell KL, Ghetti B, Goedert M, Scheres SHW. Cryo-EM structures of Aβ40 filaments from the leptomeninges of individuals with Alzheimer's disease and cerebral amyloid angiopathy. Acta Neuropathol Commun 2023;11:191. https://doi.org/10.1186/s40478-023-01694-8.

[37] Leistner C, Wilkinson M, Burgess A, Lovatt M, Goodbody S, Xu Y, Deuchars S, Radford SE, Ranson NA, Frank RAW. The in-tissue molecular architecture of β-amyloid pathology in the mammalian brain. Nat Commun 2023;14:2833. https://doi.org/10.1038/s41467-023-38495-5.

[38] Tarutani A, Lövestam S, Zhang X, Kotecha A, Robinson AC, Mann DMA, Saito Y, Murayama S, Tomita T, Goedert M, Scheres S, Hasegawa M. Cryo-EM structures of tau filaments from SH-SY5Y cells seeded with brain extracts from cases of Alzheimer's disease and corticobasal degeneration 2023. https://doi.org/10.1101/2023.04.13.536725.

[39] Stern AM, Yang Y, Jin S, Yamashita K, Meunier AL, Liu W, Cai Y, Ericsson M, Liu L, Goedert M, Scheres SHW, Selkoe DJ. Abundant Aβ fibrils in ultracentrifugal supernatants of aqueous extracts from Alzheimer's disease brains. Neuron 2023;111:2012-2020.e4. https://doi.org/10.1016/j.neuron.2023.04.007.

[40] Gilbert MAG, Fatima N, Jenkins J, O'Sullivan TJ, Schertel A, Halfon Y, Wilkinson M, Morrema THJ, Geibel M, Read RJ, Ranson NA, Radford SE, Hoozemans JJM, Frank RAW. CryoET of β-amyloid and tau within postmortem Alzheimer's disease brain. Nature 2024;631:913–9. https://doi.org/10.1038/s41586-024-07680-x.

[41] Baumeister W. From proteomic inventory to architecture. FEBS Lett 2005;579:933–7. https://doi.org/10.1016/j.febslet.2004.10.102.

[42] Frank J. Approaches to large-scale structures. Curr Opin Struct Biol 1995;5:194–201. https://doi.org/10.1016/0959-440x(95)80075-1.

[43] McCafferty CL, Klumpe S, Amaro RE, Kukulski W, Collinson L, Engel BD. Integrating cellular electron microscopy with multimodal data to explore biology across space and time. Cell 2024;187:563–84. https://doi.org/10.1016/j.cell.2024.01.005.

[44] Nogales E, Mahamid J. Bridging structural and cell biology with cryo-electron microscopy. Nature 2024;628:47–56. https://doi.org/10.1038/s41586-024-07198-2.

[45] Kühlbrandt W. The Resolution Revolution. Science 2014;343:1443–4. https://doi.org/10.1126/science.1251652.

[46] Bäuerlein FJB, Fernández-Busnadiego R, Baumeister W. Investigating the Structure of Neurotoxic Protein Aggregates Inside Cells. Trends Cell Biol 2020;30:951–66. https://doi.org/10.1016/j.tcb.2020.08.007.

[47] Lovatt M, Leistner C, Frank RAW. Bridging length scales from molecules to the whole organism by cryoCLEM and cryoET. Faraday Discuss 2022;240:114–26. https://doi.org/10.1039/d2fd00081d.

[48] Caspy I, Wang Z, Bharat TAM. Structural biology inside multicellular specimens using electron cryotomography. Q Rev Biophys 2025;58:e6. https://doi.org/10.1017/s0033583525000010.

[49] Klumpe S, Plitzko JM. Cryo-focused ion beam milling for cryo-electron tomography: Shaping the future of in situ structural biology. Curr Opin Struct Biol 2025;94:103138. https://doi.org/10.1016/j.sbi.2025.103138.

[50] Frank RAW, Komiyama NH, Ryan TJ, Zhu F, O'Dell TJ, Grant SGN. NMDA receptors are selectively partitioned into complexes and supercomplexes during synapse maturation. Nat Commun 2016;7:11264. https://doi.org/10.1038/ncomms11264.

[51] Zhu F, Cizeron M, Qiu Z, Benavides-Piccione R, Kopanitsa MV, Skene NG, Koniaris B, DeFelipe J, Fransén E, Komiyama NH, Grant SGN. Architecture of the Mouse Brain Synaptome. Neuron 2018;99:781-799.e10. https://doi.org/10.1016/j.neuron.2018.07.007.

[52] Unterauer EM, Boushehri SS, Jevdokimenko K, Masullo LA, Ganji M, Sograte-Idrissi S, Kowalewski R, Strauss S, Reinhardt SCM, Perovic A, Marr C, Opazo F, Fornasiero EF, Jungmann R. Spatial proteomics in neurons at single-protein resolution. Cell 2024;187:1785-1800.e16. https://doi.org/10.1016/j.cell.2024.02.045.

[53] Hickey SM, Ung B, Bader C, Brooks R, Lazniewska J, Johnson IRD, Sorvina A, Logan J, Martini C, Moore CR, Karageorgos L, Sweetman MJ, Brooks DA. Fluorescence Microscopy—An Outline of Hardware, Biological Handling, and Fluorophore Considerations. Cells 2021;11:35. https://doi.org/10.3390/cells11010035.

[54] Ting JT, Lee BR, Chong P, Soler-Llavina G, Cobbs C, Koch C, Zeng H, Lein E. Preparation of Acute Brain Slices Using an Optimized N-Methyl-D-glucamine Protective Recovery Method. J Vis Exp : JoVE 2018:53825. https://doi.org/10.3791/53825.

[55] Dorris DM, Hauser CA, Minnehan CE, Meitzen J. An aerator for brain slice experiments in individual cell culture plate wells. J Neurosci Methods 2014;238:1–10. https://doi.org/10.1016/j.jneumeth.2014.09.017.

[56] Dubochet J, Adrian M, Chang J-J, Homo J-C, Lepault J, McDowall AW, Schultz P. Cryo-electron microscopy of vitrified specimens. Q Rev Biophys 1988;21:129–228. https://doi.org/10.1017/s0033583500004297.

[57] Dubochet J, Blanc NS. The cell in absence of aggregation artifacts. Micron 2001;32:91–9. https://doi.org/10.1016/s0968-4328(00)00026-3.

[58] Medalia O, Weber I, Frangakis AS, Nicastro D, Gerisch G, Baumeister W. Macromolecular Architecture in Eukaryotic Cells Visualized by Cryoelectron Tomography. Science 2002;298:1209–13. https://doi.org/10.1126/science.1076184.

[59] McDowall AW, Chang J -J., Freeman R, Lepault J, Walter CA, Dubochet J. Electron microscopy of frozen hydrated sections of vitreous ice and vitrified biological samples. J Microsc 1983;131:1–9. https://doi.org/10.1111/j.1365-2818.1983.tb04225.x.

[60] Zuber B, Nikonenko I, Klauser P, Muller D, Dubochet J. The mammalian central nervous synaptic cleft contains a high density of periodically organized complexes. Proc Natl Acad Sci 2005;102:19192–7. https://doi.org/10.1073/pnas.0509527102.

[61] Barnard T, Gupta BL, Hall TA. Effects of the high-molecular-weight cryoprotectant dextran on fluid secretion by Calliphora salivary glands. Cryobiology 1984;21:559–69. https://doi.org/10.1016/0011-2240(84)90055-5.

[62] Peukes J, Lovatt C, Leistner C, Boulanger J, Morado DR, Fuller MJ, Kukulski W, Zhu F, Komiyama NH, Briggs JA, Grant SG, Frank RA. The molecular infrastructure of glutamatergic synapses in the mammalian forebrain. eLife 2025;13:RP100335. https://doi.org/10.7554/elife.100335.

[63] Pöge M, Dickmanns M, Xu P, Li M, Schiøtz OH, Kaiser COJ, Ma J, Bieber A, Capitanio C, Brenner J, Riggi M, Klumpe S, Miras M, Jasemi NSK, Schulze WX, Simon R, Frommer WB, Plitzko JM, Baumeister W. Making plant tissue accessible for cryo-electron tomography. bioRxiv 2025:2025.02.14.638237. https://doi.org/10.1101/2025.02.14.638237.

[64] Dubochet J. The Physics of Rapid Cooling and Its Implications for Cryoimmobilization of Cells. Methods Cell Biol 2007;79:7–21. https://doi.org/10.1016/s0091-679x(06)79001-x.

[65] Wu S, Armache J-P, Cheng Y. Single-particle cryo-EM data acquisition by using direct electron detection camera. J Electron Microsc 2015;65:35–41. https://doi.org/10.1093/jmicro/dfv355.

[66] Neselu K, Wang B, Rice WJ, Potter CS, Carragher B, Chua EYD. Measuring the effects of ice thickness on resolution in single particle cryo-EM. J Struct Biol: X 2023;7:100085. https://doi.org/10.1016/j.yjsbx.2023.100085.

[67] Al-Amoudi A, Norlen LPO, Dubochet J. Cryo-electron microscopy of vitreous sections of native biological cells and tissues. J Struct Biol 2004;148:131–5. https://doi.org/10.1016/j.jsb.2004.03.010.

[68] Studer D, Klein A, Iacovache I, Gnaegi H, Zuber B. A new tool based on two micromanipulators facilitates the handling of ultrathin cryosection ribbons. J Struct Biol 2014;185:125–8. https://doi.org/10.1016/j.jsb.2013.11.005.

[69] Pierson J, Fernández JJ, Bos E, Amini S, Gnaegi H, Vos M, Bel B, Adolfsen F, Carrascosa JL, Peters PJ. Improving the technique of vitreous cryo-sectioning for cryo-electron tomography: Electrostatic charging for section attachment and implementation of an anti-contamination glove box. J Struct Biol 2010;169:219–25. https://doi.org/10.1016/j.jsb.2009.10.001.

[70] Marko M, Hsieh C, Schalek R, Frank J, Mannella C. Focused-ion-beam thinning of frozen-hydrated biological specimens for cryo-electron microscopy. Nat Methods 2007;4:215–7. https://doi.org/10.1038/nmeth1014.

[71] Overwijk MHF, Heuvel FC van den, Bulle-Lieuwma CWT. Novel scheme for the preparation of transmission electron microscopy specimens with a focused ion beam. J Vac Sci Technol B: Microelectron Nanometer Struct Process, Meas, Phenom 1993;11:2021–4. https://doi.org/10.1116/1.586537.

[72] Rigort A, Bäuerlein FJB, Leis A, Gruska M, Hoffmann C, Laugks T, Böhm U, Eibauer M, Gnaegi H, Baumeister W, Plitzko JM. Micromachining tools and correlative approaches for cellular cryo-electron tomography. J Struct Biol 2010;172:169–79. https://doi.org/10.1016/j.jsb.2010.02.011.

[73] Rubino S, Akhtar S, Melin P, Searle A, Spellward P, Leifer K. A site-specific focused-ion-beam lift-out method for cryo Transmission Electron Microscopy. J Struct Biol 2012;180:572–6. https://doi.org/10.1016/j.jsb.2012.08.012.

[74] Mahamid J, Schampers R, Persoon H, Hyman AA, Baumeister W, Plitzko JM. A focused ion beam milling and lift-out approach for site-specific preparation of frozen-hydrated lamellas from multicellular organisms. J Struct Biol 2015;192:262–9. https://doi.org/10.1016/j.jsb.2015.07.012.

[75] Schaffer M, Mahamid J, Engel BD, Laugks T, Baumeister W, Plitzko JM. Optimized cryo-focused ion beam sample preparation aimed at in situ structural studies of membrane proteins. J Struct Biol 2017;197:73–82. https://doi.org/10.1016/j.jsb.2016.07.010.

[76] Schaffer M, Pfeffer S, Mahamid J, Kleindiek S, Laugks T, Albert S, Engel BD, Rummel A, Smith AJ, Baumeister W, Plitzko JM. A cryo-FIB lift-out technique enables molecular-resolution cryo-ET within native Caenorhabditis elegans tissue. Nat Methods 2019;16:757–62. https://doi.org/10.1038/s41592-019-0497-5.

[77] Schaffer M, Mahamid J, Engel BD, Laugks T, Baumeister W, Plitzko JM. Optimized cryo-focused ion beam sample preparation aimed at in situ structural studies of membrane proteins. J Struct Biol 2017;197:73–82. https://doi.org/10.1016/j.jsb.2016.07.010.

[78] Tacke S, Erdmann P, Wang Z, Klumpe S, Grange M, Plitzko J, Raunser S. A streamlined workflow for automated cryo focused ion beam milling. J Struct Biol 2021;213:107743. https://doi.org/10.1016/j.jsb.2021.107743.

[79] Nguyen HTD, Perone G, Klena N, Vazzana R, Don FK, Silva M, Sorrentino S, Swuec P, Leroux F, Kalebic N, Coscia F, Erdmann PS. Serialized on-grid lift-in sectioning for tomography (SOLIST) enables a biopsy at the nanoscale. Nat Methods 2024;21:1693–701. https://doi.org/10.1038/s41592-024-02384-6.

[80] Schiøtz OH, Kaiser CJO, Klumpe S, Morado DR, Poege M, Schneider J, Beck F, Klebl DP, Thompson C, Plitzko JM. Serial Lift-Out: sampling the molecular anatomy of whole organisms. Nat Methods 2024;21:1684–92. https://doi.org/10.1038/s41592-023-02113-5.

[81] Han HM, Zuber B, Dubochet J. Compression and crevasses in vitreous sections under different cutting conditions. J Microsc 2008;230:167–71. https://doi.org/10.1111/j.1365-2818.2008.01972.x.

[82] Ericson ML, Lindberg H. Design and potential of instrumented ultramicrotomy. Polymer 1997;38:4485–9. https://doi.org/10.1016/s0032-3861(96)01051-8.

[83] Elferich J, Kaminek M, Kong L, Odriozola A, Kukulski W, Zuber B, Grigorieff N. In situ high-resolution cryo-EM reconstructions from CEMOVIS. IUCrJ 2025;12:502–10. https://doi.org/10.1107/s2052252525005196.

[84] Al-Amoudi A, Baradaran R, Yuan X, Naschberger A. In situ structure of bacterial 50S ribosomes at 2.98 Å resolution from vitreous sections. bioRxiv 2025:2025.06.03.657669. https://doi.org/10.1101/2025.06.03.657669.

[85] Berger C, Dumoux M, Glen T, Yee NB -y., Mitchels JM, Patáková Z, Darrow MC, Naismith JH, Grange M. Plasma FIB milling for the determination of structures in situ. Nat Commun 2023;14:629. https://doi.org/10.1038/s41467-023-36372-9.

[86] Lucas BA, Grigorieff N. Quantification of gallium cryo-FIB milling damage in biological lamellae. Proc Natl Acad Sci 2023;120:e2301852120. https://doi.org/10.1073/pnas.2301852120.

[87] Yang Q, Wu C, Zhu D, Li J, Cheng J, Zhang X. The reduction of FIB damage on cryo-lamella by lowering energy of ion beam revealed by a quantitative analysis. Structure 2023;31:1275-1281.e4. https://doi.org/10.1016/j.str.2023.07.002.

[88] Matsui A, Spangler C, Elferich J, Shiozaki M, Jean N, Zhao X, Qin M, Zhong H, Yu Z, Gouaux E. Cryo-electron tomographic investigation of native hippocampal glutamatergic synapses. eLife 2024;13:RP98458. https://doi.org/10.7554/elife.98458.

[89] Glynn C, Smith JLR, Case M, Csöndör R, Katsini A, Sanita ME, Glen TS, Pennington A, Grange M. A generalizable and targeted molecular biopsy approach for in situ cryogenic

electron tomography of vitreous brain tissue. Cell Rep Methods 2025;5:101080. https://doi.org/10.1016/j.crmeth.2025.101080.

[90] Sartori A, Gatz R, Beck F, Rigort A, Baumeister W, Plitzko JM. Correlative microscopy: Bridging the gap between fluorescence light microscopy and cryo-electron tomography. J Struct Biol 2007;160:135–45. https://doi.org/10.1016/j.jsb.2007.07.011.

[91] Schwartz CL, Sarbash VI, Ataullakhanov FI, McIntosh JR, Nicastro D. Cryo-fluorescence microscopy facilitates correlations between light and cryo-electron microscopy and reduces the rate of photobleaching. J Microsc 2007;227:98–109. https://doi.org/10.1111/j.1365-2818.2007.01794.x.

[92] Briegel A, Chen S, Koster AJ, Plitzko JM, Schwartz CL, Jensen GJ. Chapter Thirteen Correlated Light and Electron Cryo-Microscopy. Methods Enzym 2010;481:317–41. https://doi.org/10.1016/s0076-6879(10)81013-4.

[93] Arnold J, Mahamid J, Lucic V, de Marco A, Fernandez J-J, Laugks T, Mayer T, Hyman AA, Baumeister W, Plitzko JM. Site-Specific Cryo-focused Ion Beam Sample Preparation Guided by 3D Correlative Microscopy. Biophys J 2016;110:860–9. https://doi.org/10.1016/j.bpj.2015.10.053.

[94] Wu G-H, Mitchell PG, Galaz-Montoya JG, Hecksel CW, Sontag EM, Gangadharan V, Marshman J, Mankus D, Bisher ME, Lytton-Jean AKR, Frydman J, Czymmek K, Chiu W. Multi-scale 3D Cryo-Correlative Microscopy for Vitrified Cells. Structure 2020;28:1231-1237.e3. https://doi.org/10.1016/j.str.2020.07.017.

[95] Dahlberg PD, Perez D, Su Z, Chiu W, Moerner WE. Cryogenic Correlative Single-Particle Photoluminescence Spectroscopy and Electron Tomography for Investigation of Nanomaterials. Angew Chem Int Ed 2020;59:15642–8. https://doi.org/10.1002/anie.202002856.

[96] Last MGF, Voortman LM, Sharp TH. Building a super-resolution fluorescence cryomicroscope. Methods Cell Biol 2024;187:205–22. https://doi.org/10.1016/bs.mcb.2024.02.026.

[97] Stillman JM, Lopes FM, Lin J-P, Hu K, Reich DS, Schafer DP. Lipofuscin-like autofluorescence within microglia and its impact on studying microglial engulfment. Nat Commun 2023;14:7060. https://doi.org/10.1038/s41467-023-42809-y.

[98] Gorelick S, Buckley G, Gervinskas G, Johnson TK, Handley A, Caggiano MP, Whisstock JC, Pocock R, Marco A de. PIE-scope, integrated cryo-correlative light and FIB/SEM microscopy. eLife 2019;8:e45919. https://doi.org/10.7554/elife.45919.

[99] DeRosier DJ, Klug A. Reconstruction of Three Dimensional Structures from Electron Micrographs. Nature 1968;217:130–4. https://doi.org/10.1038/217130a0.

[100] Hoppe W, Langer R, Knesch G, Poppe Ch. Protein-Kristallstrukturanalyse mit Elektronenstrahlen. Naturwissenschaften 1968;55:333–6. https://doi.org/10.1007/bf00600449.

[101] Henderson R. The potential and limitations of neutrons, electrons and X-rays for atomic resolution microscopy of unstained biological molecules. Q Rev Biophys 1995;28:171–93. https://doi.org/10.1017/s003358350000305x.

[102] Glaeser RM. Limitations to significant information in biological electron microscopy as a result of radiation damage. J Ultrastruct Res 1971;36:466–82. https://doi.org/10.1016/s0022-5320(71)80118-1.

[103] Glaeser RM, Hagen WJH, Han B-G, Henderson R, McMullan G, Russo CJ. Defocus-dependent Thon-ring fading. Biorxiv 2020:2020.10.12.336214. https://doi.org/10.1101/2020.10.12.336214.

[104] Brilot AF, Chen JZ, Cheng A, Pan J, Harrison SC, Potter CS, Carragher B, Henderson R, Grigorieff N. Beam-induced motion of vitrified specimen on holey carbon film. J Struct Biol 2012;177:630–7. https://doi.org/10.1016/j.jsb.2012.02.003.

[105] Campbell MG, Cheng A, Brilot AF, Moeller A, Lyumkis D, Veesler D, Pan J, Harrison SC, Potter CS, Carragher B, Grigorieff N. Movies of Ice-Embedded Particles Enhance Resolution in Electron Cryo-Microscopy. Structure 2012;20:1823–8. https://doi.org/10.1016/j.str.2012.08.026.

[106] Li X, Mooney P, Zheng S, Booth CR, Braunfeld MB, Gubbens S, Agard DA, Cheng Y. Electron counting and beam-induced motion correction enable near-atomic-resolution single-particle cryo-EM. Nat Methods 2013;10:584–90. https://doi.org/10.1038/nmeth.2472.

[107] Bharat TAM, Russo CJ, Löwe J, Passmore LA, Scheres SHW. Advances in Single-Particle Electron Cryomicroscopy Structure Determination applied to Sub-tomogram Averaging. Structure 2015;23:1743–53. https://doi.org/10.1016/j.str.2015.06.026.

[108] Hagen WJH, Wan W, Briggs JAG. Implementation of a cryo-electron tomography tilt-scheme optimized for high resolution subtomogram averaging. J Struct Biol 2017;197:191–8. https://doi.org/10.1016/j.jsb.2016.06.007.

[109] Tuijtel MW, Majtner T, Turoňová B, Beck M. Optimal tilt-increment for cryo-ET. bioRxiv 2025:2025.08.20.671201. https://doi.org/10.1101/2025.08.20.671201.

[110] Erickson HP, Klug A. Measurement and compensation of defocusing and aberrations by Fourier processing of electron micrographs. Philosophical Transactions Royal Soc Lond B Biological Sci 1971;261:105–18. https://doi.org/10.1098/rstb.1971.0040.

[111] Weis F, Hagen WJH. Combining high throughput and high quality for cryo-electron microscopy data collection. Acta Crystallogr Sect D 2020;76:724–8. https://doi.org/10.1107/s2059798320008347.

[112] Glaeser RM, Hagen WJH, Han B-G, Henderson R, McMullan G, Russo CJ. Defocus-dependent Thon-ring fading. Ultramicroscopy 2021;222:113213. https://doi.org/10.1016/j.ultramic.2021.113213.

[113] Bouvette J, Liu H-F, Du X, Zhou Y, Sikkema AP, Mello J da FR e, Klemm BP, Huang R, Schaaper RM, Borgnia MJ, Bartesaghi A. Beam image-shift accelerated data acquisition

for near-atomic resolution single-particle cryo-electron tomography. Nat Commun 2021;12:1957. https://doi.org/10.1038/s41467-021-22251-8.

[114] Eisenstein F, Yanagisawa H, Kashihara H, Kikkawa M, Tsukita S, Danev R. Parallel cryo electron tomography on in situ lamellae. Nat Methods 2023;20:131–8. https://doi.org/10.1038/s41592-022-01690-1.

[115] Peck A, Carter SD, Mai H, Chen S, Burt A, Jensen GJ. Montage electron tomography of vitrified specimens. J Struct Biol 2022;214:107860. https://doi.org/10.1016/j.jsb.2022.107860.

[116] Yang JE, Larson MR, Sibert BS, Kim JY, Parrell D, Sanchez JC, Pappas V, Kumar A, Cai K, Thompson K, Wright ER. Correlative montage parallel array cryo-tomography for in situ structural cell biology. Nat Methods 2023;20:1537–43. https://doi.org/10.1038/s41592-023-01999-5.

[117] Rickgauer JP, Grigorieff N, Denk W. Single-protein detection in crowded molecular environments in cryo-EM images. eLife 2017;6:e25648. https://doi.org/10.7554/elife.25648.

[118] Zheng W, Chai P, Zhu J, Zhang K. High-resolution in situ structures of mammalian respiratory supercomplexes. Nature 2024;631:232–9. https://doi.org/10.1038/s41586-024-07488-9.

[119] Sanchez RM, Zhang Y, Chen W, Dietrich L, Kudryashev M. Subnanometer-resolution structure determination in situ by hybrid subtomogram averaging - single particle cryo-EM. Nat Commun 2020;11:3709. https://doi.org/10.1038/s41467-020-17466-0.

[120] Lucas BA, Himes BA, Xue L, Grant T, Mahamid J, Grigorieff N. Locating macromolecular assemblies in cells by 2D template matching with cisTEM. eLife 2021;10:e68946. https://doi.org/10.7554/elife.68946.

[121] Zheng SQ, Palovcak E, Armache J-P, Verba KA, Cheng Y, Agard DA. MotionCor2: anisotropic correction of beam-induced motion for improved cryo-electron microscopy. Nat Methods 2017;14:331–2. https://doi.org/10.1038/nmeth.4193.

[122] Kremer JR, Mastronarde DN, McIntosh JR. Computer Visualization of Three-Dimensional Image Data Using IMOD. J Struct Biol 1996;116:71–6. https://doi.org/10.1006/jsbi.1996.0013.

[123] Mastronarde DN, Held SR. Automated tilt series alignment and tomographic reconstruction in IMOD. J Struct Biol 2017;197:102–13. https://doi.org/10.1016/j.jsb.2016.07.011.

[124] Wan W, Briggs JAG. Chapter Thirteen Cryo-Electron Tomography and Subtomogram Averaging. Methods Enzym 2016;579:329–67. https://doi.org/10.1016/bs.mie.2016.04.014.

[125] Tegunov D, Cramer P. Real-time cryo-electron microscopy data preprocessing with Warp. Nat Methods 2019;16:1146–52. https://doi.org/10.1038/s41592-019-0580-y.

[126] Tegunov D, Xue L, Dienemann C, Cramer P, Mahamid J. Multi-particle cryo-EM refinement with M visualizes ribosome-antibiotic complex at 3.5 Å in cells. Nat Methods 2021;18:186–93. https://doi.org/10.1038/s41592-020-01054-7.

[127] Zheng S, Wolff G, Greenan G, Chen Z, Faas FGA, Bárcena M, Koster AJ, Cheng Y, Agard DA. AreTomo: An integrated software package for automated marker-free, motion-corrected cryo-electron tomographic alignment and reconstruction. J Struct Biol: X 2022;6:100068. https://doi.org/10.1016/j.yjsbx.2022.100068.

[128] Tao C-L, Liu Y-T, Sun R, Zhang B, Qi L, Shivakoti S, Tian C-L, Zhang P, Lau P-M, Zhou ZH, Bi G-Q. Differentiation and Characterization of Excitatory and Inhibitory Synapses by Cryo-electron Tomography and Correlative Microscopy. J Neurosci 2018;38:1493–510. https://doi.org/10.1523/jneurosci.1548-17.2017.

[129] Zila V, Margiotta E, Turoňová B, Müller TG, Zimmerli CE, Mattei S, Allegretti M, Börner K, Rada J, Müller B, Lusic M, Kräusslich H-G, Beck M. Cone-shaped HIV-1 capsids are transported through intact nuclear pores. Cell 2021;184:1032-1046.e18. https://doi.org/10.1016/j.cell.2021.01.025.

[130] Delarue M, Brittingham GP, Pfeffer S, Surovtsev IV, Pinglay S, Kennedy KJ, Schaffer M, Gutierrez JI, Sang D, Poterewicz G, Chung JK, Plitzko JM, Groves JT, Jacobs-Wagner C, Engel BD, Holt LJ. mTORC1 Controls Phase Separation and the Biophysical Properties of the Cytoplasm by Tuning Crowding. Cell 2018;174:338-349.e20. https://doi.org/10.1016/j.cell.2018.05.042.

[131] Bykov YS, Schaffer M, Dodonova SO, Albert S, Plitzko JM, Baumeister W, Engel BD, Briggs JA. The structure of the COPI coat determined within the cell. Elife 2017;6:e32493. https://doi.org/10.7554/elife.32493.

[132] Lamm L, Zufferey S, Zhang H, Righetto RD, Waltz F, Wietrzynski W, Yamauchi KA, Burt A, Liu Y, Martinez-Sanchez A, Ziegler S, Isensee F, Schnabel JA, Engel BD, Peng T. MemBrain v2: an end-to-end tool for the analysis of membranes in cryo-electron tomography. bioRxiv 2025:2024.01.05.574336. https://doi.org/10.1101/2024.01.05.574336.

[133] Peck A, Yu Y, Schwartz J, Cheng A, Ermel UH, Kandel S, Kimanius D, Montabana E, Serwas D, Siems H, Wang F, Zhao Z, Zheng S, Haury M, Agard D, Potter C, Carragher B, Harrington K, Paraan M. Annotating CryoET Volumes: A Machine Learning Challenge. bioRxiv 2024:2024.11.04.621686. https://doi.org/10.1101/2024.11.04.621686.

[134] Chen M, Dai W, Sun SY, Jonasch D, He CY, Schmid MF, Chiu W, Ludtke SJ. Convolutional neural networks for automated annotation of cellular cryo-electron tomograms. Nature Methods 2017;14:983–5.

[135] Vilas JL, Oton J, Messaoudi C, Melero R, Conesa P, Ramirez-Aportela E, Mota J, Martinez M, Jimenez A, Marabini R, Carazo JM, Vargas J, Sorzano COS. Measurement of local resolution in electron tomography. J Struct Biology X 2020;4:100016. https://doi.org/10.1016/j.yjsbx.2019.100016.

[136] Kukulski W, Schorb M, Welsch S, Picco A, Kaksonen M, Briggs JAG. Correlated fluorescence and 3D electron microscopy with high sensitivity and spatial precision. J Cell Biol 2011;192:111–9. https://doi.org/10.1083/jcb.201009037.

[137] Chaumont F de, Dallongeville S, Chenouard N, Hervé N, Pop S, Provoost T, Meas-Yedid V, Pankajakshan P, Lecomte T, Montagner YL, Lagache T, Dufour A, Olivo-Marin J-C. Icy: an open bioimage informatics platform for extended reproducible research. Nat Methods 2012;9:690–6. https://doi.org/10.1038/nmeth.2075.

[138] Schorb M, Gaechter L, Avinoam O, Sieckmann F, Clarke M, Bebeacua C, Bykov YS, Sonnen AF-P, Lihl R, Briggs JAG. New hardware and workflows for semi-automated correlative cryo-fluorescence and cryo-electron microscopy/tomography. J Struct Biol 2017;197:83–93. https://doi.org/10.1016/j.jsb.2016.06.020.

[139] Paul-Gilloteaux P, Heiligenstein X, Belle M, Domart M-C, Larijani B, Collinson L, Raposo G, Salamero J. eC-CLEM: flexible multidimensional registration software for correlative microscopies. Nat Methods 2017;14:102–3. https://doi.org/10.1038/nmeth.4170.

[140] Kudryashev M, Castaño-Díez D, Stahlberg H. Limiting factors in single particle cryo electron tomography. Comput Struct Biotechnol J 2012;1:e201207002. https://doi.org/10.5936/csbj.201207002.

[141] Förster F, Medalia O, Zauberman N, Baumeister W, Fass D. Retrovirus envelope protein complex structure in situ studied by cryo-electron tomography. Proc Natl Acad Sci 2005;102:4729–34. https://doi.org/10.1073/pnas.0409178102.

[142] Himes BA, Zhang P. emClarity: software for high-resolution cryo-electron tomography and subtomogram averaging. Nat Methods 2018;15:955–61. https://doi.org/10.1038/s41592-018-0167-z.

[143] Zivanov J, Otón J, Ke Z, Kügelgen A von, Pyle E, Qu K, Morado D, Castaño-Díez D, Zanetti G, Bharat TA, Briggs JA, Scheres SH. A Bayesian approach to single-particle electron cryo-tomography in RELION-4.0. eLife 2022;11:e83724. https://doi.org/10.7554/elife.83724.

[144] Liu H-F, Zhou Y, Huang Q, Piland J, Jin W, Mandel J, Du X, Martin J, Bartesaghi A. nextPYP: a comprehensive and scalable platform for characterizing protein variability in situ using single-particle cryo-electron tomography. Nat Methods 2023;20:1909–19. https://doi.org/10.1038/s41592-023-02045-0.

[145] Burt A, Toader B, Warshamanage R, Kügelgen A von, Pyle E, Zivanov J, Kimanius D, Bharat TAM, Scheres SHW. An image processing pipeline for electron cryo-tomography in RELION-5. FEBS Open Bio 2024;14:1788–804. https://doi.org/10.1002/2211-5463.13873.

[146] Castaño-Díez D, Kudryashev M, Arheit M, Stahlberg H. Dynamo: A flexible, user-friendly development tool for subtomogram averaging of cryo-EM data in high-performance computing environments. J Struct Biol 2012;178:139–51. https://doi.org/10.1016/j.jsb.2011.12.017.

[147] Chen M, Bell JM, Shi X, Sun SY, Wang Z, Ludtke SJ. A complete data processing workflow for CryoET and subtomogram averaging. Nat Methods 2019;16:1161–8. https://doi.org/10.1038/s41592-019-0591-8.

[148] Wagner T, Merino F, Stabrin M, Moriya T, Antoni C, Apelbaum A, Hagel P, Sitsel O, Raisch T, Prumbaum D, Quentin D, Roderer D, Tacke S, Siebolds B, Schubert E, Shaikh TR, Lill P, Gatsogiannis C, Raunser S. SPHIRE-crYOLO is a fast and accurate fully automated particle picker for cryo-EM. Commun Biol 2019;2:218. https://doi.org/10.1038/s42003-019-0437-z.

[149] Rice G, Wagner T, Stabrin M, Sitsel O, Prumbaum D, Raunser S. TomoTwin: generalized 3D localization of macromolecules in cryo-electron tomograms with structural data mining. Nat Methods 2023;20:871–80. https://doi.org/10.1038/s41592-023-01878-z.

[150] Ermel UH, Arghittu SM, Frangakis AS. ArtiaX: An electron tomography toolbox for the interactive handling of sub-tomograms in UCSF ChimeraX. Protein Sci 2022;31:e4472. https://doi.org/10.1002/pro.4472.

[151] Martinez-Sanchez A, Kochovski Z, Laugks U, Borgloh JM zum A, Chakraborty S, Pfeffer S, Baumeister W, Lučić V. Template-free detection and classification of membrane-bound complexes in cryo-electron tomograms. Nat Methods 2020;17:209–16. https://doi.org/10.1038/s41592-019-0675-5.

[152] Hrabe T, Chen Y, Pfeffer S, Cuellar LK, Mangold A-V, Förster F. PyTom: A python-based toolbox for localization of macromolecules in cryo-electron tomograms and subtomogram analysis. J Struct Biol 2012;178:177–88. https://doi.org/10.1016/j.jsb.2011.12.003.

[153] Teresa-Trueba I de, Goetz SK, Mattausch A, Stojanovska F, Zimmerli CE, Toro-Nahuelpan M, Cheng DWC, Tollervey F, Pape C, Beck M, Diz-Muñoz A, Kreshuk A, Mahamid J, Zaugg JB. Convolutional networks for supervised mining of molecular patterns within cellular context. Nat Methods 2023;20:284–94. https://doi.org/10.1038/s41592-022-01746-2.

[154] Wagner T, Lusnig L, Pospich S, Stabrin M, Schönfeld F, Raunser S. Two particle-picking procedures for filamentous proteins: SPHIRE-crYOLO filament mode and SPHIRE-STRIPER. Acta Crystallogr Sect D 2020;76:613–20. https://doi.org/10.1107/s2059798320007342.

[155] Goddard TD, Huang CC, Meng EC, Pettersen EF, Couch GS, Morris JH, Ferrin TE. UCSF ChimeraX: Meeting modern challenges in visualization and analysis. Protein Sci 2018;27:14–25. https://doi.org/10.1002/pro.3235.

[156] Förster F, Medalia O, Zauberman N, Baumeister W, Fass D. Retrovirus envelope protein complex structure in situ studied by cryo-electron tomography. Proc Natl Acad Sci 2005;102:4729–34. https://doi.org/10.1073/pnas.0409178102.

[157] Nicastro D, Schwartz C, Pierson J, Gaudette R, Porter ME, McIntosh JR. The Molecular Architecture of Axonemes Revealed by Cryoelectron Tomography. Science 2006;313:944–8. https://doi.org/10.1126/science.1128618.

[158] Heumann JM, Hoenger A, Mastronarde DN. Clustering and variance maps for cryo-electron tomography using wedge-masked differences. J Struct Biol 2011;175:288–99. https://doi.org/10.1016/j.jsb.2011.05.011.

[159] Grant T, Rohou A, Grigorieff N. cisTEM, user-friendly software for single-particle image processing. eLife 2018;7:e35383. https://doi.org/10.7554/elife.35383.

[160] Sorzano COS, Marabini R, Velázquez-Muriel J, Bilbao-Castro JR, Scheres SHW, Carazo JM, Pascual-Montano A. XMIPP: a new generation of an open-source image processing package for electron microscopy. J Struct Biol 2004;148:194–204. https://doi.org/10.1016/j.jsb.2004.06.006.

[161] Scheres SHW. A Bayesian View on Cryo-EM Structure Determination. J Mol Biol 2012;415:406–18. https://doi.org/10.1016/j.jmb.2011.11.010.

[162] Förster F. Subtomogram analysis: The sum of a tomogram's particles reveals molecular structure in situ. J Struct Biol: X 2022;6:100063. https://doi.org/10.1016/j.yjsbx.2022.100063.

[163] Zhang X, Mahamid J. Protocol for subtomogram averaging of helical filaments in cryo-electron tomography. STAR Protoc 2024;5:103272. https://doi.org/10.1016/j.xpro.2024.103272.

[164] Cochran W, Crick FH, Vand V. The structure of synthetic polypeptides. I. The transform of atoms on a helix. Acta Crystallogr 1952;5:581–6. https://doi.org/10.1107/s0365110x52001635.

[165] Klug A, Crick FHC, Wyckoff HW. Diffraction by helical structures. Acta Crystallogr 1958;11:199–213. https://doi.org/10.1107/s0365110x58000517.

[166] Nicastro D, Schwartz C, Pierson J, Gaudette R, Porter ME, McIntosh JR. The Molecular Architecture of Axonemes Revealed by Cryoelectron Tomography. Science 2006;313:944–8. https://doi.org/10.1126/science.1128618.

[167] He S, Scheres SHW. Helical reconstruction in RELION. J Struct Biol 2017;198:163–76. https://doi.org/10.1016/j.jsb.2017.02.003.

[168] Scheres SHW. Amyloid structure determination in RELION-3.1. Acta Crystallogr Sect D 2020;76:94–101. https://doi.org/10.1107/s2059798319016577.

[169] Xing H, Taniguchi R, Khusainov I, Kreysing JP, Welsch S, Turoňová B, Beck M. Translation dynamics in human cells visualized at high resolution reveal cancer drug action. Science 2023;381:70–5. https://doi.org/10.1126/science.adh1411.

[170] You X, Zhang X, Cheng J, Xiao Y, Ma J, Sun S, Zhang X, Wang H-W, Sui S-F. In situ structure of the red algal phycobilisome–PSII–PSI–LHC megacomplex. Nature 2023;616:199–206. https://doi.org/10.1038/s41586-023-05831-0.

[171] Wagner J, Carvajal AI, Bracher A, Beck F, Wan W, Bohn S, Körner R, Baumeister W, Fernandez-Busnadiego R, Hartl FU. Visualizing chaperonin function in situ by cryo-electron tomography. Nature 2024;633:459–64. https://doi.org/10.1038/s41586-024-07843-w.

[172] Watanabe R, Zyla D, Parekh D, Hong C, Jones Y, Schendel SL, Wan W, Castillon G, Saphire EO. Intracellular Ebola virus nucleocapsid assembly revealed by in situ cryo-electron tomography. Cell 2024;187:5587-5603.e19. https://doi.org/10.1016/j.cell.2024.08.044.

[173] Wang Y, Li S, Mokbel M, May AI, Liang Z, Zeng Y, Wang W, Zhang H, Yu F, Sporbeck K, Jiang L, Aland S, Agudo-Canalejo J, Knorr RL, Fang X. Biomolecular condensates mediate bending and scission of endosome membranes. Nature 2024;634:1204–10. https://doi.org/10.1038/s41586-024-07990-0.

[174] Arakhamia T, Lee CE, Carlomagno Y, Kumar M, Duong DM, Wesseling H, Kundinger SR, Wang K, Williams D, DeTure M, Dickson DW, Cook CN, Seyfried NT, Petrucelli L, Steen JA, Fitzpatrick AWP. Posttranslational Modifications Mediate the Structural Diversity of Tauopathy Strains. Cell 2021;184:6207–10. https://doi.org/10.1016/j.cell.2021.11.029.

[175] Lövestam S, Wagstaff JL, Katsinelos T, Shi J, Freund SMV, Goedert M, Scheres SHW. Twelve phosphomimetic mutations induce the assembly of recombinant full-length human tau into paired helical filaments. bioRxiv 2025:2024.10.23.619846. https://doi.org/10.1101/2024.10.23.619846.

[176] Crowther RA. Straight and paired helical filaments in Alzheimer disease have a common structural unit. Proc Natl Acad Sci 1991;88:2288–92. https://doi.org/10.1073/pnas.88.6.2288.

[177] Scheres SHW. RELION: Implementation of a Bayesian approach to cryo-EM structure determination. J Struct Biol 2012;180:519–30. https://doi.org/10.1016/j.jsb.2012.09.006.

[178] Kleywegt GJ, Adams PD, Butcher SJ, Lawson CL, Rohou A, Rosenthal PB, Subramaniam S, Topf M, Abbott S, Baldwin PR, Berrisford JM, Bricogne G, Choudhary P, Croll TI, Danev R, Ganesan SJ, Grant T, Gutmanas A, Henderson R, Heymann JB, Huiskonen JT, Istrate A, Kato T, Lander GC, Lok S-M, Ludtke SJ, Murshudov GN, Pye R, Pintilie GD, Richardson JS, Sachse C, Salih O, Scheres SHW, Schroeder GF, Sorzano COS, Stagg SM, Wang Z, Warshamanage R, Westbrook JD, Winn MD, Young JY, Burley SK, Hoch JC, Kurisu G, Morris K, Patwardhan A, Velankar S. Community recommendations on cryoEM data archiving and validation. IUCrJ 2024;11:140–51. https://doi.org/10.1107/s2052252524001246.

[179] Jones TA, Zou J -Y., Cowan SW, Kjeldgaard M. Improved methods for building protein models in electron density maps and the location of errors in these models. Acta Crystallogr Sect A 1991;47:110–9. https://doi.org/10.1107/s0108767390010224.

[180] Topf M, Lasker K, Webb B, Wolfson H, Chiu W, Sali A. Protein Structure Fitting and Refinement Guided by Cryo-EM Density. Structure 2008;16:295–307. https://doi.org/10.1016/j.str.2007.11.016.

[181] Joseph AP, Malhotra S, Burnley T, Wood C, Clare DK, Winn M, Topf M. Refinement of atomic models in high resolution EM reconstructions using Flex-EM and local assessment. Methods 2016;100:42–9. https://doi.org/10.1016/j.ymeth.2016.03.007.

[182] Beton JG, Mulvaney T, Cragnolini T, Topf M. Cryo-EM structure and B-factor refinement with ensemble representation. Nat Commun 2024;15:444. https://doi.org/10.1038/s41467-023-44593-1.

[183] Schur FKM, Obr M, Hagen WJH, Wan W, Jakobi AJ, Kirkpatrick JM, Sachse C, Kräusslich H-G, Briggs JAG. An atomic model of HIV-1 capsid-SP1 reveals structures regulating assembly and maturation. Science 2016;353:506–8. https://doi.org/10.1126/science.aaf9620.

[184] Pintilie G, Zhang K, Su Z, Li S, Schmid MF, Chiu W. Measurement of atom resolvability in cryo-EM maps with Q-scores. Nat Methods 2020;17:328–34. https://doi.org/10.1038/s41592-020-0731-1.

[185] Pintilie G, Shao C, Wang Z, Hudson BP, Flatt JW, Schmid MF, Morris KL, Burley SK, Chiu W. Q-score as a reliability measure for protein, nucleic acid and small-molecule atomic coordinate models derived from 3DEM maps. Acta Crystallogr Sect D 2025;81:410–22. https://doi.org/10.1107/s2059798325005923.

[186] Rosenthal PB, Henderson R. Optimal Determination of Particle Orientation, Absolute Hand, and Contrast Loss in Single-particle Electron Cryomicroscopy. J Mol Biol 2003;333:721–45. https://doi.org/10.1016/j.jmb.2003.07.013.

[187] Millán C, McCoy AJ, Terwilliger TC, Read RJ. Likelihood-based docking of models into cryo-EM maps. Acta Crystallogr Sect D 2023;79:281–9. https://doi.org/10.1107/s2059798323001602.

[188] Read RJ, Millán C, McCoy AJ, Terwilliger TC. Likelihood-based signal and noise analysis for docking of models into cryo-EM maps. Acta Crystallogr Sect D 2023;79:271–80. https://doi.org/10.1107/s2059798323001596.

[189] Read RJ, Pettersen EF, McCoy AJ, Croll TI, Terwilliger TC, Poon BK, Meng EC, Liebschner D, Adams PD. Likelihood-based interactive local docking into cryo-EM maps in ChimeraX. Acta Crystallogr Sect D 2024;80:588–98. https://doi.org/10.1107/s2059798324006776.

[190] Müller H, Jin J, Danev R, Spence J, Padmore H, Glaeser RM. Design of an electron microscope phase plate using a focused continuous-wave laser. N J Phys 2010;12:073011. https://doi.org/10.1088/1367-2630/12/7/073011.

[191] Schwartz O, Axelrod JJ, Campbell SL, Turnbaugh C, Glaeser RM, Müller H. Laser phase plate for transmission electron microscopy. Nat Methods 2019;16:1016–20. https://doi.org/10.1038/s41592-019-0552-2.

[192] Du DX, Fitzpatrick AWP. Design of an ultrafast pulsed ponderomotive phase plate for cryo-electron tomography. Cell Rep Methods 2023;3:100387. https://doi.org/10.1016/j.crmeth.2022.100387.

[193] Axelrod JJ, Zhang JT, Petrov PN, Glaeser RM, Müller H. Modern approaches to improving phase contrast electron microscopy. Curr Opin Struct Biol 2024;86:102805. https://doi.org/10.1016/j.sbi.2024.102805.

[194] Küçükoğlu B, Mohammed I, Guerrero-Ferreira RC, Ribet SM, Varnavides G, Leidl ML, Lau K, Nazarov S, Myasnikov A, Kube M, Radecke J, Sachse C, Müller-Caspary K, Ophus C, Stahlberg H. Low-dose cryo-electron ptychography of proteins at sub-nanometer resolution. Nat Commun 2024;15:8062. https://doi.org/10.1038/s41467-024-52403-5.

[195] Zhou L, Song J, Kim JS, Pei X, Huang C, Boyce M, Mendonça L, Clare D, Siebert A, Allen CS, Liberti E, Stuart D, Pan X, Nellist PD, Zhang P, Kirkland AI, Wang P. Low-dose phase retrieval of biological specimens using cryo-electron ptychography. Nat Commun 2020;11:2773. https://doi.org/10.1038/s41467-020-16391-6.

[196] Wu J, Liu C, Wang AJ, Gao YZ, Fu LT, Liu Z, Dickerson JL, Russo CJ, Wang P. Chromatic aberration (Cc) corrected cryo-EM: The structure of pseudorabies virus (PRV) using both zero-loss and energy loss electrons. Ultramicroscopy 2025;276:114182. https://doi.org/10.1016/j.ultramic.2025.114182.

[197] Dickerson JL, Naydenova K, Peet MJ, Wilson H, Nandy B, McMullan G, Morrison R, Russo CJ. Reducing the effects of radiation damage in cryo-EM using liquid helium temperatures. Proc Natl Acad Sci 2025;122:e2421538122. https://doi.org/10.1073/pnas.2421538122.

[198] Schertel A, Snaidero N, Han H-M, Ruhwedel T, Laue M, Grabenbauer M, Möbius W. Cryo FIB-SEM: Volume imaging of cellular ultrastructure in native frozen specimens. J Struct Biol 2013;184:355–60. https://doi.org/10.1016/j.jsb.2013.09.024.

[199] Dumoux M, Glen T, Smith JL, Ho EM, Perdigão LM, Pennington A, Klumpe S, Yee NB, Farmer DA, Lai PY, Bowles W, Kelley R, Plitzko JM, Wu L, Basham M, Clare DK, Siebert CA, Darrow MC, Naismith JH, Grange M. Cryo-plasma FIB/SEM volume imaging of biological specimens. eLife 2023;12:e83623. https://doi.org/10.7554/elife.83623.

[200] Larabell CA, Nugent KA. Imaging cellular architecture with X-rays. Curr Opin Struct Biol 2010;20:623–31. https://doi.org/10.1016/j.sbi.2010.08.008.

[201] Fahy K, Weinhardt V, Vihinen-Ranta M, Fletcher N, Skoko D, Pereiro E, Gastaminza P, Bartenschlager R, Scholz D, Ekman A, McEnroe T. Compact Cell Imaging Device (CoCID) provides insights into the cellular origins of viral infections. J Phys: Photonics 2021;3:031002. https://doi.org/10.1088/2515-7647/abfc5a.

[202] Fahy K, Kapishnikov S, Donnellan M, McEnroe T, O'Reilly F, Fyans W, Sheridan P. Laboratory based correlative cryo-soft X-ray tomography and cryo-fluorescence microscopy. Methods Cell Biol 2024;187:293–320. https://doi.org/10.1016/bs.mcb.2024.02.033.

[203] Wu G-H, Mitchell PG, Galaz-Montoya JG, Hecksel CW, Sontag EM, Gangadharan V, Marshman J, Mankus D, Bisher ME, Lytton-Jean AKR, Frydman J, Czymmek K, Chiu W. Multi-scale 3D Cryo-Correlative Microscopy for Vitrified Cells. Structure 2020;28:1231-1237.e3. https://doi.org/10.1016/j.str.2020.07.017.

[204] Mendonça L, Howe A, Gilchrist JB, Sheng Y, Sun D, Knight ML, Zanetti-Domingues LC, Bateman B, Krebs A-S, Chen L, Radecke J, Li VD, Ni T, Kounatidis I, Koronfel MA, Szynkiewicz M, Harkiolaki M, Martin-Fernandez ML, James W, Zhang P. Correlative multi-scale cryo-imaging unveils SARS-CoV-2 assembly and egress. Nat Commun 2021;12:4629. https://doi.org/10.1038/s41467-021-24887-y.

[205] Elbaum M, Seifer S, Houben L, Wolf SG, Rez P. Toward Compositional Contrast by Cryo-STEM. Acc Chem Res 2021;54:3621–31. https://doi.org/10.1021/acs.accounts.1c00279.

[206] Wolf SG, Mutsafi Y, Dadosh T, Ilani T, Lansky Z, Horowitz B, Rubin S, Elbaum M, Fass D. 3D visualization of mitochondrial solid-phase calcium stores in whole cells. eLife 2017;6:e29929. https://doi.org/10.7554/elife.29929.

[207] Ochner H, Isbilir B, Blasche S, Scheidweiler D, Zhang Y, Wang Z, Smith T, Franco C, Bradley R, Patil KR, Bharat TAM. Sub-cellular chemical mapping in bacteria using correlated cryogenic electron and mass spectrometry imaging. bioRxiv 2025:2025.08.29.673036. https://doi.org/10.1101/2025.08.29.673036.

[208] Passarelli MK, Pirkl A, Moellers R, Grinfeld D, Kollmer F, Havelund R, Newman CF, Marshall PS, Arlinghaus H, Alexander MR, West A, Horning S, Niehuis E, Makarov A, Dollery CT, Gilmore IS. The 3D OrbiSIMS—label-free metabolic imaging with subcellular lateral resolution and high mass-resolving power. Nat Methods 2017;14:1175–83. https://doi.org/10.1038/nmeth.4504.

[209] Mastronarde DN. Dual-Axis Tomography: An Approach with Alignment Methods That Preserve Resolution. J Struct Biol 1997;120:343–52. https://doi.org/10.1006/jsbi.1997.3919.

[210] Read RJ, Millán C, McCoy AJ, Terwilliger TC. Robust and efficient likelihood-based docking of models into cryo-EM reconstructions. Acta Crystallogr Sect A Found Adv 2023;79:C16–C16. https://doi.org/10.1107/s205327332309592x.